

Member : Junru Zhu

参赛队员姓名: 朱俊儒

School : Pegasus California School

中学: 青岛博格思学校

Province : Shandong

省份: 山东

Country/Region : China

国家/地区: 中国

Supervisors : Yongqiang Zhu

指导教师姓名: 朱永强

Supervisors : Pingxia Zhang

指导教师姓名: 张平霞

Topic: Obstacle Avoidance Control for Multi-Axle and Multi-Steering-Mode Wheeled Robot Based on Window-Zone Division Strategy

论文题目: 基于窗口-区域划分策略的多轴多模式转向轮式机器人避障控制

丘成桐中学科学奖-学术诚信声明

本参赛团队郑重声明：

1. 参赛团队提交的参赛队员和指导老师信息完整且属实无误。
2. 所提交的研究报告是在指导老师指导下进行的研究工作和取得的研究成果。
3. 尽本团队所知，除文中加以标注和致谢中所罗列的内容外，研究中不包含其他人已经发表或撰写过的研究成果，不存在代写或其他违规行为。

以上，若有不实之处，本人愿意承担一切相关责任，并服从丘成

桐中学科学奖组织委员会的裁决。

我校全名是青岛市即墨区博格思文化培训学校有限公司，简称青岛博格思学校，在教体部门和工商部门分别进行了合法注册。因学校性质为营利性质，所以必须在工商部门注册，故校名中带有“有限公司”。

参赛学生（签字）：朱俊儒

本校指导老师（签字）：

学校名称（加盖学校或教务处公章）：

青岛博格思学校
Pegasus California School

外校指导老师（签字）：朱永强

单位名称（加盖单位公章）：张平霞

青岛理工大学机械与汽车工程学院

2021年 9月 11日

Abstract

At present, most autonomous obstacle avoidance robots have circular bodies, and there are few researches about autonomous long body multi-axle wheeled robots. Due to the longer body, multiple number of wheels and the complexity of controlling, it is difficult for a multi-axle wheeled robot to avoid obstacles autonomously in a narrow space when the space passage width is less than the robot body length. To solve this problem, this article presents three strategies for local obstacle avoidance. Firstly, a multi-steering-mode control strategy based on front and rear virtual wheels is proposed. Secondly, according to the influence degree of lidar points on the robot, combining with the human driving characteristics of avoiding obstacles, a window-zone division strategy is proposed. The lidar points are selected and divided according to the degree of emergency. By eliminating irrelevant points, the work of obstacle avoidance calculation is reduced. Thus, this increases the response speed of obstacle avoidance. Thirdly, the driving trajectory prediction and the gap-seeking theory of normal obstacle avoidance is proposed. By calculating the relationship between the lidar points of the obstacle and the trajectory coverage area, the iterative calculation of the obstacle avoidance scheme for the proposed steering is carried out, and the feasible obstacle avoidance scheme is obtained. It can seek the passable gap among the surrounding lidar points according to the prediction of the robot's driving trajectory corresponding to different steering angles. Then, the on-board control system and the upper computer program of the robot were designed. The mechanical structure, hardware, and software control system of a five-axle wheeled robot are designed. Finally, to verify the effectiveness of the obstacle avoidance strategy, obstacle avoidance experiments were carried out based on AWS (All-Wheel-Steering) and traditional NAWS (Non-All-Wheel-Steering) with Z-shaped obstacle distribution of different passage widths. The results confirm that the proposed control strategy can realize the obstacle avoidance driving in a passage narrower than the robot body length, and the obstacle avoidance algorithm has very fast real-time performance. To verify the robustness of the control strategy, other obstacle avoidance experiments are also carried out with S-shaped, U-Shaped, and Random obstacle distribution. The results show that the proposed strategy can finish all obstacle avoidance successfully.

Keywords: Obstacle avoidance, Window-zone division strategy, Driving trajectory prediction, Gap-seeking theory, Autonomous multi-axle wheeled robot, All-wheel steering, Multi-steering-mode.

Catalogue

Abstract.....	1
1. Introduction	1
2. Robot Architecture.....	3
2.1 Mechanical Design	3
2.2 Hardware Components	4
3. Multi-Steering-Mode Control Strategy Based on Front and Rear Virtual Wheels	5
4. Windows-Zones Obstacle Avoidance Control Theory.....	9
4.1 Window-Zone Division Strategy	10
4.2 The Yellow-Window Obstacle Avoidance Strategy: Gap-Seeking Theory.....	11
4.3 Obstacle Avoidance Strategies in Specific Situations.....	16
5. Control System	17
5.1 On-Board Control System Program.....	17
5.2 Upper Computer Program.....	18
6. Experimental Verification	19
6.1 Z-Shaped Obstacle Distribution.....	19
6.2 S-Shaped Obstacle Distribution.....	22
6.3 U-Shaped Obstacle Distribution	25
6.4 Random Obstacle Distribution.....	26
7. Conclusion.....	29
References	30
Acknowledgments	32
Paper Detection Report.....	34

1. Introduction

A multi-axle wheeled robot has three or more axles. The robot has very strong loading capacity, good maneuverability and obstacle-surmounting ability due to the multiple number of wheels it has. It is often used in the transportation of a great amount of goods in factories opening exploration, and disaster rescues. However, because of its large size and the huge number of wheels, it leads to difficulties in autonomous obstacle avoidance control in a narrow space.

At present, many researchers have carried out researches on autonomous obstacle avoidance of wheeled robots. They mainly focus on two aspects: multi-robot swarm control^[1-4] and single robot control^[5]. Research on single robot is further divided into global path planning^[6,7] and local obstacle avoidance path planning^[8]. Robot of global path search, need to obtain the global distribution of obstacles from the starting point to destination in advance^[9]. However, for the robot of local searching, it does not know the distribution of obstacles in advance, so it can only detect the situation of obstacles around the robot and conduct autonomous obstacle avoidance while driving. There are many researchers presented various algorithms, such as Genetic algorithm^[10], Neural network^[11], Ant colony optimization algorithm^[12], Fuzzy logic^[13], Neuro-fuzzy^[14], Simulated annealing algorithm^[15], and Particle swarm optimization algorithm^[16], etc. But these studies do not consider obstacle avoidance in narrow areas.

To realize autonomous obstacle avoidance, the robot needs to determine the relationship between itself and the surrounding obstacles through various sensors^[17-20]. At present, the commonly used sensors are infrared sensors, ultrasonic sensors, vision sensors and laser radar sensors. Infrared sensors are seldom used because of their narrow detection range and tendency to be disturbed easily. Ultrasonic sensors can only detect the distance of obstacles in the conical area, but cannot accurately determine the angle of obstacles, so they cannot be used for accurate obstacle avoidance control. In addition, the current algorithm cannot accurately determine the position of the obstacle through the vision sensor, so in obstacle avoidance control, the vision sensor is mostly used in conjunction with other sensors. At present, the lidar sensor is relatively more mature and can accurately determine the position of obstacles, therefore it is used widely in obstacle avoidance control^[21, 22]. Moreover, 2D (2 dimensional) lidar is relatively cheaper and has a very high cost-efficient performance, which makes it be used widely^[23-27]. Therefore, we use 2D lidar as the detection sensor in this paper.

When avoiding obstacles, the robot needs to make real-time decisions according to the distribution of obstacles. Therefore, the response time of the obstacle avoidance action determines the maximum speed of the robot's autonomous driving. To accelerate the obstacle avoidance speed and realize the real-time obstacle avoidance, Wu *et al.*^[28] proposed a deep reinforcement learning method ANOA (Autonomous Navigation and Obstacle Avoidance) to enhance the intelligence of unmanned surface vehicles (USVs) in the sophisticated mane environment, the ANOA algorithm is proposed for real-time path planning with obstacle avoidance. Borenstein *et al.*^[29] developed a new real-time obstacle avoidance approach for mobile robots. By permitting the detection of unknown obstacles simultaneously with the steering of the mobile robot to avoid collisions and advancing toward the target, this method can save processing time. Xu *et al.*^[30] proposed a new maximum-speed aware velocity obstacle (MVO) algorithm. It can control a mobile robot to avoid one or multiple high-speed obstacles. Zaheer *et al.*^[31] proposed a new real-time "Free-configuration Eigenspace" (FCE) technique for obstacle avoidance and navigation. The FCE enables an autonomous robot to detect unknown obstacles and avoid collisions while guiding the robot toward the target. HU *et al.*^[32] introduced an experiential aggregative reinforcement learning method based on Multi-Attribute Decision-Making. However, these studies do not consider the problem of fast obstacle avoidance for multi-axle robots.

Other researchers have studied trajectory curves of obstacle avoidance to get good performance. Akka *et al.*^[33] proposed a trajectory tracking control method for mobile robot when there are static obstacles on the reference trajectory. The tracking control is based on the fuzzy parallel distribution compensation scheme and the linear quadratic controller is used as the state feedback controller of each subsystem. By fully considering the non-

holonomic constraints of mobile robot systems, Yuan *et al.* [34] propose a new quadrupole potential field method to plan collision-free trajectories. However, these studies do not consider the problem of robot trajectory control in multi-mode steering.

Most of the robots used in the above research have round (Figure 1 (A), (B) (G), (H), (I)) or square (Figure 1 (C) (D), (E), (F)) bodies and few of them are multi-axle wheeled robots with long bodies. These obstacle avoidance strategies are very suitable when the length and width of the robot are almost equal or the shape of the robot is close to a circle. However, for the multi-axle robot, its body length is much larger than its width. Therefore, the obstacle avoidance control becomes very complex compared with the wheeled robot with a general circular body. The multi-axle robot will occupy more space and has larger turning radius while turning. Therefore, it is urgent to propose a new obstacle avoidance method combining the characteristics of the long body, so as to realize the obstacle avoidance in a narrow space. Then it can reflect the mobility and flexibility of the long body robot.

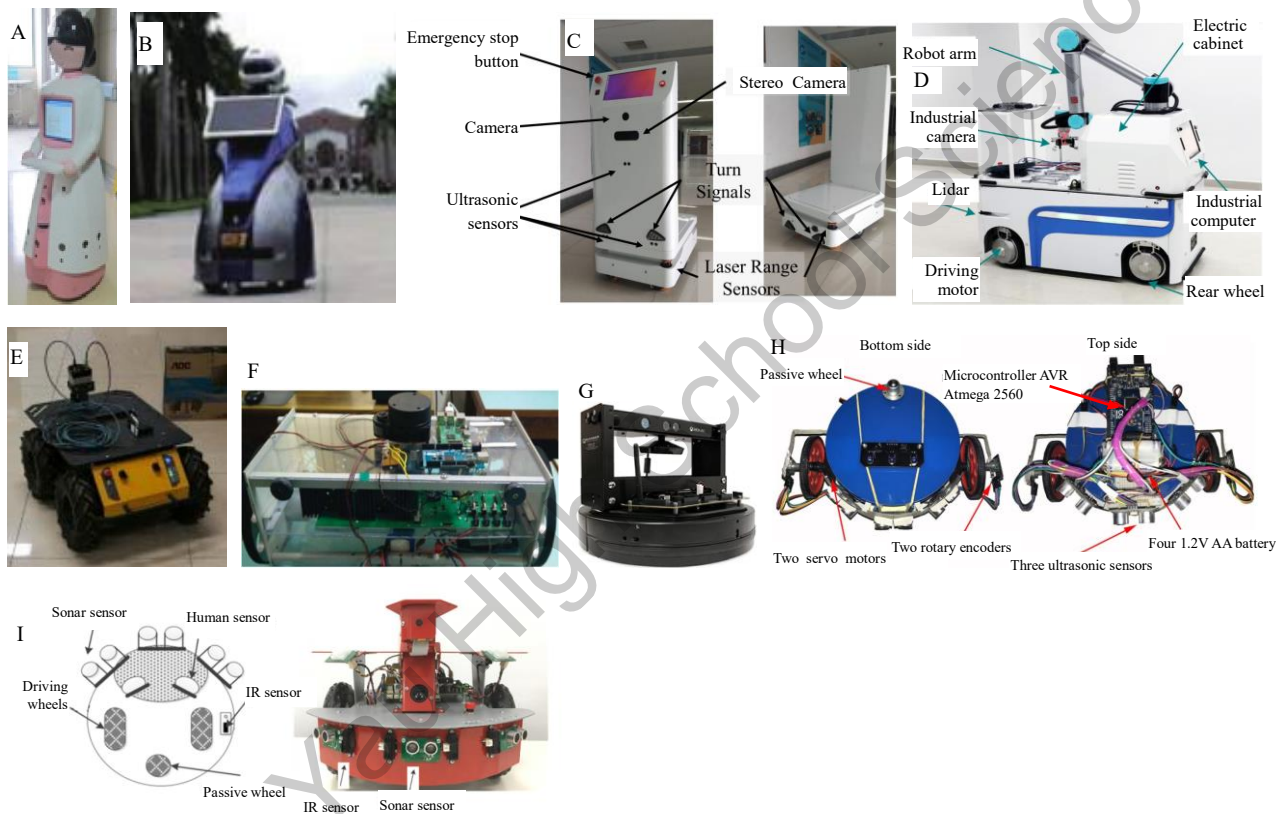


FIGURE 1: Obstacle avoidance robots of various shapes. (A) Robot using 2D laser-vision obstacle detection developed by Shandong University [35]. (B) NTU-I robot developed by National Taiwan University [36]. (C) Differential drive robot developed by University of Science and Technology of China [37]. (D) A four-wheeled steerable mobile robot developed by Huazhong University of Science and Technology [38]. (E) Husky Robot developed by University of Electronic Science and Technology of China [39]. (F) Mobile Robot developed by National Institute of Technology Tiruchirappalli Tiruchirappalli [40]. (G) Robot used by Institute of Electrical Engineering [41]. (H) Mobile robot designed by University of Basrah [42]. (I) Circular non-holonomic mobile robot Dr. Robot X80 used by Institute of Information Science, Academia Sinica, Taiwan [43].

At present, most robots can only turn their front wheels or part of wheels, which results in low flexibility and requires a large turning space. Therefore, some studies have been carried out from the perspective of wheel steering control, Xie *et al.* [38] present an enhanced coupled fractional-order sliding mode control (CFSMC) framework for trajectory tracking control of four-wheeled steerable mobile robots (FSMR) with the ability of collision avoidance. It can ensure faster obstacle avoidance convergence and shorter distances when comparing with traditional methods. Lin *et al.* [44] propose a multi-wheel steering logistics robot that can move collision-free into any pallet that has not

been precisely placed. Prasad [45] propose autonomous velocity and steering angle controllers for the car-like tractor robot such that the tractor-trailer system moves from an initial position to a designated target. The proposed method simultaneously takes into account the dynamics constraints of the system and also ensures that the robot avoids any fixed obstacles on its way to the target. However, these studies do not consider the multi-mode steering problem of the multi-axle robot.

The multi-axle robot has a longer body and more wheels. In this case, if we can control the steering of each wheel individually, especially for different steering modes used in the different distribution of obstacles, it will significantly reduce the difficulty of obstacle avoidance. Moreover, the space occupation will be reduced and the flexibility will be improved.

In addition, in the actual obstacle avoidance, the robot's obstacle avoidance algorithm cannot occupy too much time, otherwise it will affect the moving speed. Therefore, it is necessary to study the fast and autonomous obstacle avoidance in a narrow space in combination with a long body of the multi-axle wheeled robot. To solve these problems, we proposed a new obstacle avoidance control strategy for multi-steering-mode based on window-zone and gap-seeking theory. Then we designed a five-axle wheeled robot with a long body, and all wheels can steer independently for experiments.

The rest of this article is organized as follows: Firstly, the mechanical structure and hardware circuit of a lidar robot used in the obstacle avoidance experiment are analyzed in the second section. Secondly, we propose multi-steering-mode control strategy based on front and rear virtual wheels in the third section. To ensure the symmetry of the trajectory and easy to be controlled, we propose to set the virtual steering wheels at the midpoint of the first and last axles of the robot. Thirdly, we propose three strategies in the fourth section. They are the window-zone division strategy, gap-seeking method, and obstacle avoidance strategies for special distribution of obstacles. Fourthly, the on-board control system and the upper computer control system of the robot are introduced in the fifth section. On this basis, in order to verify the proposed methods, the experiments of obstacle avoidance with different distribution of obstacles, such as Z-shaped, S-shaped, U-shaped, and Random obstacle distribution, are carried out in the sixth section. In Z-shaped obstacle distribution, several different passage width experiments are carried out. To verify the effect of the control algorithm, AWS (All-Wheel-Steering) and traditional NAWS (Non-All-Wheel-Steering) strategy are compared. Conclusion are given in the seventh section.

2. Robot Architecture

2.1 Mechanical Design

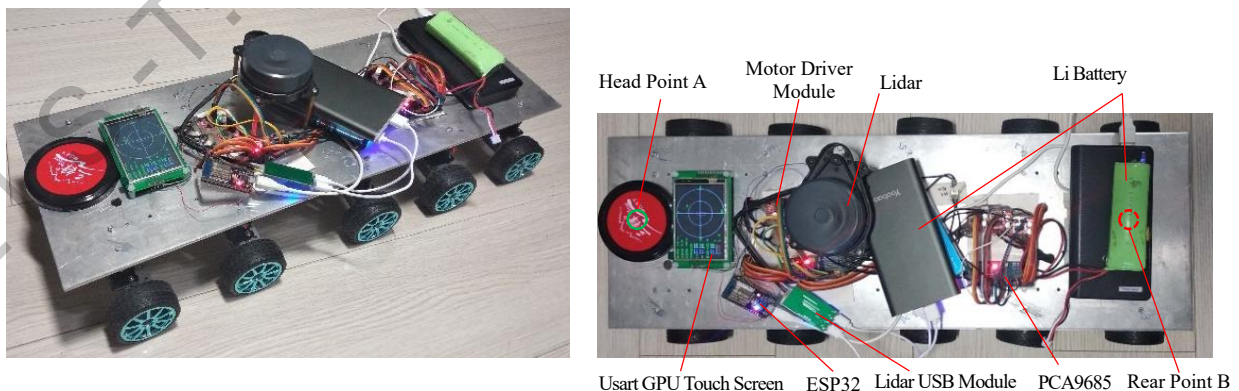


FIGURE 2: The architecture of five-axle wheeled robot for research.

The mechanical dimension of the robot is 250mm×600mm in Figure 2. The robot has 10 wheels, and each wheel has

two motors, as shown in Figure 3. One is steering servo motor for driving wheel to steer, and another is wheel-driving motor for driving wheel to roll [46]. The steering servo is fixed to the robot body through the steering gear plate. The wheel-driving motor is fixed on the steering gear plate. In this way, the steering servo can drive the wheel-driving motor, and wheels to realize the robot steering through the steering gear plate. Hence, every wheel has two degrees of freedom.

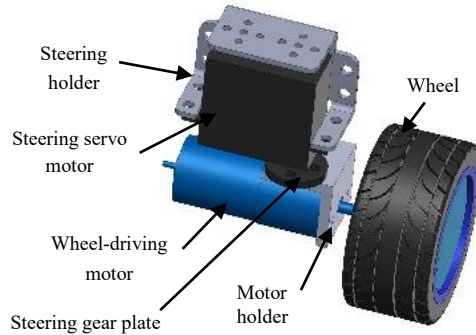


FIGURE 3: Wheel system structure

2.2 Hardware Components

The hardware circuit of the wheeled robot is composed of steering servo, lidar, wheel driving motor, DC motor & wheel, motor driving module (L298N), PCA9685, ESP32S, USART GPU serial communication touch screen, and 7.4V3000mAH30C Li Battery, as shown in Figure 4.

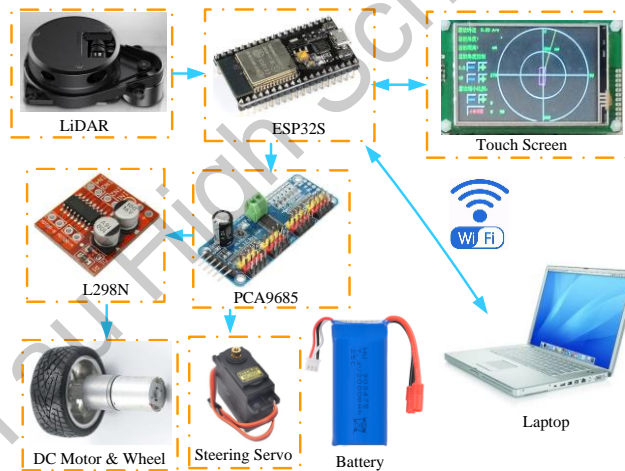


FIGURE 4: Hardware structure of the five-axle all-wheel-steering wheeled robot.

The core control unit is ESP32S, which is responsible for transmitting lidar signals to the laptop through WIFI and receiving autonomous obstacle avoidance instructions from the laptop. The ESP32S communicates with the lidar through a serial port to obtain the distance and angle information of the surrounding obstacles. ESP32S and the serial touch screen communicate through another serial communication port to display the information of the surrounding obstacles in real-time. We can set the displayed information through the screen. ESP32S communicates with the PCA9685 module through the I²C bus. PCA9685 module controls the steering servo of each wheel in PWM mode to realize the control of wheel steering angle. At the same time, the speed of each wheel driving motor is controlled to meet the requirement of the wheel driving speed. Because each wheel is driven by two actuators, we can independently control the steering angle, driving speed, and direction of each wheel. Then we can achieve very flexible multi-steering modes, such as non-steering first-axle wheel mode, non-steering last-axle wheel mode, lateral travel mode, situ rotation mode, and adverse-phase steering mode, etc. For cost-efficient purposes, the obstacle

detection module adopted by the system is a Delta-2B laser radar, with a range is 0.2 ~ 8m, a scanning range of 360° and a resolution of about 0.592°. The system rotates once to generate 608 pairs of lidar data points including angles and distances, which can be used to employ the algorithms used for obstacle detection and obstacle avoidance. The rotation speed is 5 ~ 10 r/s, so the interval time is about 100~200ms. Therefore, the control unit is needed to calculate the next movement direction of the robot according to these lidar points of obstacles within 100ms. The mounting position of the lidar was on top of the robot body to achieve a proper and unobstructed plane of measurement.

3. Multi-Steering-Mode Control Strategy Based on Front and Rear Virtual Wheels

Previous studies were based on the steering angle control of the right side wheels [46], but it is difficult to ensure the symmetry of the left and right steering trajectory. For example, in obstacle avoidance driving, the turning radius of the left turn is different from that of the right turn, which leads to the difference in the ability of obstacle avoidance. This is not good for obstacle avoidance control. To solve this problem, when the robot turns to the left or right, to ensure the symmetry of the trajectory and easy to control, we propose to set the virtual steering wheels at the midpoint of the first and last axles of the robot, as shown in Figure 5-9.

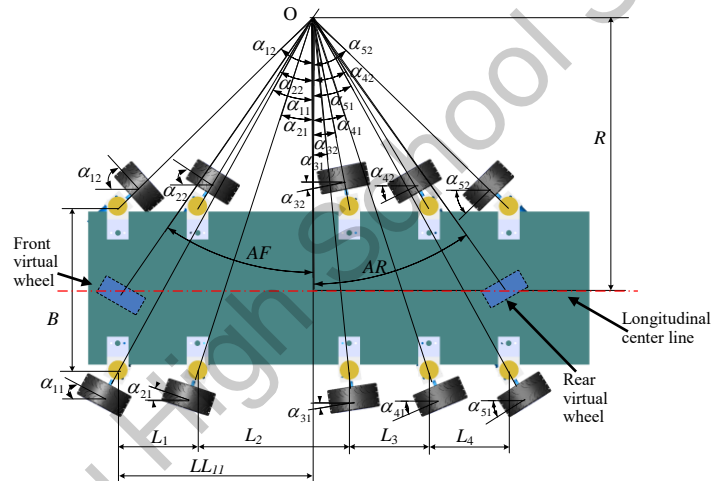


FIGURE 5: Geometric relation diagram of the robot wheels' steering angles.

From Figure 5, it can be seen:

$$\begin{aligned} \tan(AF/180\pi) &= \frac{LL_{11}}{R} \\ \tan(-AR/180\pi) &= \frac{\sum_{i=1}^{n-1} L_i - LL_{11}}{R} \\ R &= \frac{LL_{11}}{\tan(AF/180\pi)} = \frac{\sum_{i=1}^{n-1} L_i - LL_{11}}{\tan(-AR/180\pi)} \end{aligned} \quad (1)$$

Where LL_{11} is the distance between the turning center point O and the first axle of the robot projected on the longitudinal center line of the robot. AF and AR are the steering angles of the front and rear virtual wheels on the center of the first axle and last axle, respectively. The unit is degree. When the wheels are steering clockwise, the angle is positive; otherwise, it is negative. R is the distance between the turning center point O and the longitudinal center axis of the robot body. L_i is the distance between the i th and $(i+1)$ th axle. n is the number of robot axles, in this paper, $n=5$.

According to equation (1), the distance between the turning center point O and the first axle of the robot is projected on the longitudinal center line of the robot as:

$$LL_{11} = \sum_{j=1}^{n-1} L_i \frac{\tan(AF/180\pi)}{\tan(AF/180\pi) - \tan(AR/180\pi)} \quad (2)$$

The distance between the turning center point O and the longitudinal center axis of the robot body is

$$R = \begin{cases} LL_{11}/\tan(AF/180\pi) & AF \neq 0 \\ (\sum_{i=1}^{n-1} L_i - LL_{11})/\tan(-AR/180\pi) & AR \neq 0 \end{cases} \quad (3)$$

The steering angle of the j th wheel in the i th axle is:

$$\alpha_{ij} = \tan^{-1} \left(\left(LL_{11} - \sum_{k=1}^{i-1} L_k \right) / (R - (-1)^j B/2) \right) \quad (4)$$

Where α_{ij} is the steering angle of the j th wheel in the i th axle. When the wheel turns clockwise, the angle is positive; otherwise, it is negative. $i = 1, 2, \dots, n$, and $j = 1, 2$. 1 is the left wheel and 2 is the right wheel. L_k is the distance between the k th and $(k+1)$ th axle. B is the wheelbase of the left and right wheels.

The distance from the turning center point O to the j th wheel in the i th axle is:

$$R_{ij} = (R - (-1)^j B/2) / \cos(\alpha_{ij}) \quad (5)$$

The maximum radius is:

$$R_{max} = \max(|R_{11}|, |R_{12}|, |R_{51}|, |R_{52}|) \quad (6)$$

As shown in Figure 6, the relationship between wheel rotation variable *Speed* and control variable V is:

$$\begin{cases} Speed = V - 90 \\ 90 < V \leq 180, & Speed > 0, & \text{robot moves forward} \\ V = 90, & Speed = 0, & \text{robot stops} \\ 0 \leq V < 90, & Speed < 0, & \text{robot moves backward} \end{cases} \quad (7)$$

Where *Speed* is the rotation control variable of the wheel. V is the robot moving control variable of speed.

When $V=90$, wheel rotation speed is 0; When $V=180$, the wheel speed is the fastest in the forward direction, and the speed variable is V_{max} . When $V=0$, the wheel speed reaches the reverse fastest, and the variable is $-V_{max}$. Therefore, the speed of forward and reverse rotation of wheels can be controlled according to the deviation degree of V relative to 90. Where 180 and 0 correspond to the maximum speed forward and the maximum speed backward, respectively, and there is a linear correspondence between the threshold and the speed.

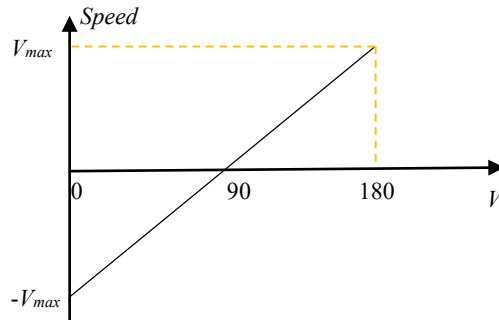


FIGURE 6: Curve relationship between *Speed* and control variable V .

Since the radius of the track circle of each wheel is different when turning, the speed of the wheel is also different, and is proportional to the radius of the track circle. According to the size of the moving radius, the program carries out the differential speed (the degree to which the speed V_{ij} deviates from the middle point 90), and the speed of the j th wheel in the i th axle is:

$$\begin{aligned} \frac{|V_{ij} - 90|}{|Speed|} &= \frac{|R_{ij}|}{R_{max}} \\ \frac{|V_{ij} - 90|}{|V - 90|} &= \frac{|R_{ij}|}{R_{max}} \\ V_{ij} &= \begin{cases} 90 + (V - 90)(|R_{ij}|/R_{max}) & V \geq 90 \\ 90 - (V - 90)(|R_{ij}|/R_{max}) & V < 90 \end{cases} \end{aligned} \quad (8)$$

Where V_{ij} is the speed of the j th wheel in the i th axle.

In this way, according to Ackerman's theorem, we can calculate the steering angles and speed of the robot's all actual wheels according to the steering angles of the two virtual wheels: AF and AR . According to the need of obstacle-avoiding steering of the robot, the following steering modes are proposed based on the front and rear virtual wheels steering angles AF and AR and moving speed V :

1) Steering Mode 1, $AF \cdot AR < 0$

This is the adverse-phase steering mode, as shown in Figure 5. At this point, the steering direction of the front and rear virtual wheels is opposite, and the actual steering direction of the front and rear wheels of the robot is also opposite. The robot can have a relatively small turning radius. Space used for steering is also small. Therefore, this mode is suitable for a relatively narrow steering space. According to equations (1) ~ (8), the steering angle of each wheel and the wheel speed differential control can be calculated.

2) Steering Mode 2, $AF = 0, AR \neq 0$

This is non-steering first-axle wheel mode, as shown in Figure 7. According to equations (1) ~ (8), the steering angle of each wheel and the wheel speed differential control can be calculated.

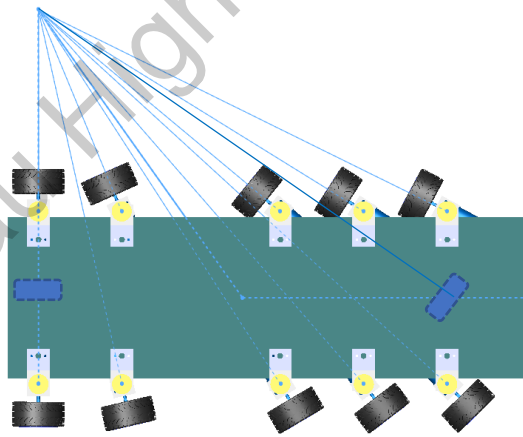


FIGURE 7: Non-steering first-axle wheel mode.

3) Steering Mode 3, $AF \neq 0, AR = 0$

This is the non-steering last-axle wheel mode, as shown in Figure 8. According to equations (1) ~ (8), the steering angle of each wheel and the wheel speed differential control can be calculated.

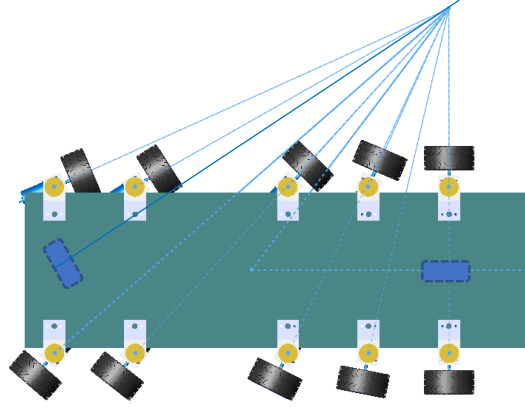


FIGURE 8: Non-steering last-axle wheel mode.

4) Steering Mode 4, $AF = 90^\circ, AR = -AF, R = 0$

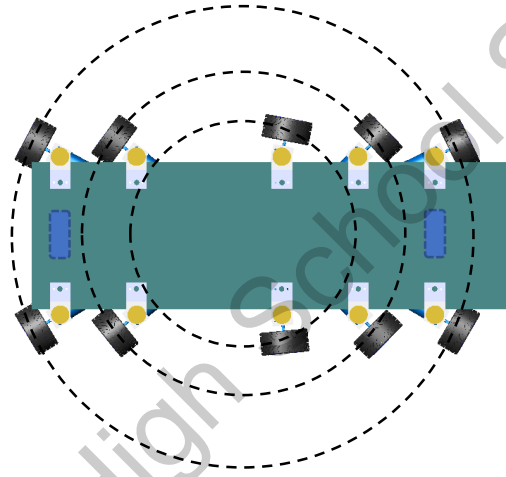


FIGURE 9: In situ rotation mode.

This is the in situ rotation state, as shown in Figure 9. The turning center is located between the 2nd and 3rd axle.

The steering angle of the j th wheel in the i th axle is:

$$\alpha_{1j} = (-1)^{j-1} \tan^{-1} \left(\left(\sum_{i=1}^{n-1} L_i / 2 \right) / B / 2 \right)$$

$$j = 1, 2$$

$$\alpha_{2j} = (-1)^{j-1} \tan^{-1} \left(\left(\sum_{i=1}^{n-1} L_i / 2 - L_1 \right) / B / 2 \right)$$

$$j = 1, 2$$

$$\alpha_{ij} = (-1)^j \tan^{-1} \left(\left(\sum_{j=1}^{n-1} L_i / 2 - \sum_{k=i}^{n-1} L_k \right) / B / 2 \right)$$

$$i = 3, 4$$

$$j = 1, 2$$

$$\begin{aligned}\alpha_{5j} &= -\alpha_{1j} \\ j &= 1,2\end{aligned}\quad (9)$$

The distance from the turning center point O to the j th wheel in the i th axle is:

$$R_{ij} = (B/2) / \cos \alpha_{ij} \quad (10)$$

According equations (6), the maximum turning radius is calculated. The speed V_{ij} of each wheel is:

$$V_{ij} = \begin{cases} 90 + (-1)^j (V - 90) (|R_{ij}| / R_{max}) & V \geq 90 \\ 90 - (-1)^j (V - 90) (|R_{ij}| / R_{max}) & V < 90 \end{cases} \quad (11)$$

5) Steering Mode 5, $AF = -90^\circ, AR = AF$

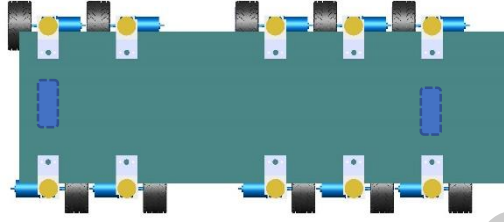


FIGURE 10: Lateral driving mode.

This is the lateral driving state of 90° , as shown in Figure 10. Wheel steering angle of the j th side in the i th axle is:

$$\alpha_{ij} = -90^\circ, i=1, 2, \dots, 5 \quad j=1,2 \quad (12)$$

Wheel speed of the j th side in the i th axle is:

$$\begin{aligned}V_{ij} &= V \\ i &= 1, 2, \dots, 5 \\ j &= 1, 2\end{aligned} \quad (13)$$

4. Windows-Zones Obstacle Avoidance Control Theory

In real life, while driving a car, the driver does not need to know generally all the information around the car. Instead, he only knows the obstacles in the next planned driving area according to the driving conditions of the car. Similarly, when the robot is running, the information of many lidar points is valueless to the robot's next running, such as lidar points that are very far away from the robot and lidar points behind the robot when moving forward, as shown in Figure 11(a). The analysis of these worthless lidar points will slow down the calculation speed of obstacle avoidance, so it is necessary to eliminate them. Based on this, the emergency obstacle avoidance control strategy based on window-zone division and the yellow zone control strategy based on gap-seeking theory are proposed. The control strategy of obstacle avoidance based on window-zone division is as follows: when the robot is running, it only pays attention to the window-zone of the next destination location to see if there are obstacles, and then takes emergency or yellow-window obstacle avoidance measures according to the influence of lidar points on the robot's moving as shown in Figure 12. By zone division, lidar points can be decreased, the work of obstacle avoidance calculation can be reduced greatly, and the response speed of obstacle avoidance can be improved. The yellow zone control strategy based on gap-seeking theory is to select lidar points, find a gap that can be passed through, and plan local obstacle avoidance routes in the normal obstacle avoidance state. It checks the gap by iteratively scanning according to the steering angle of the robot and predicts different traveling trajectories.

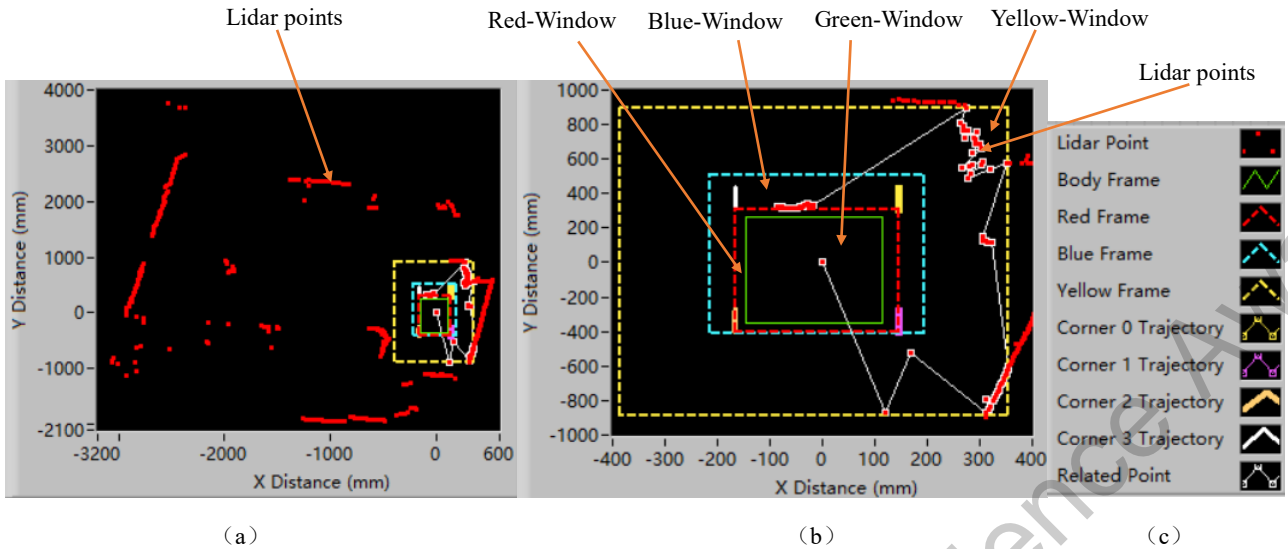


FIGURE 11: Lidar points before and after window division: (a) All 608 lidar points before the window division, (b) The remaining 74 lidar points after the window division, (c) Legends.

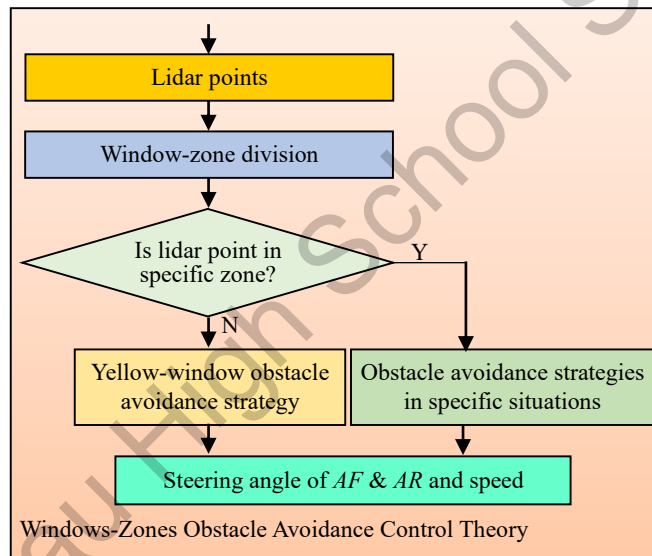


FIGURE 12: Flow chart of Windows-Zones Obstacle Avoidance Control

4.1 Window-Zone Division Strategy

Lots of lidar points around the robot are divided into four windows according to the size and urgency of the impact on the robot: green, red, blue and yellow, as shown in Figure 11(b).

The green line is the body contour line, and the area within the green line is the Green-Window, which is the highest level of obstacle avoidance control. Once the lidar point appears in this window, it indicates that there has been a serious collision. The robot should stop immediately, and then take the highest obstacle avoidance measures to control the robot away from the lidar point in this window promptly.

The area between the red line and the green line is the Red-Window, which serves as the emergency buffer area for the robot body to collide with obstacles. It is used to take emergency control measure to widen the distance between the robot body and obstacles at the fastest speed to avoid the body to collide with obstacles. This control measure is called the red emergency obstacle avoidance control strategy. It is the second priority.

The area between the blue line and the red line is the Blue-Window, which serves as the general buffer area for the

collision between the robot body and the obstacle. It is used to control the distance between the robot body and the obstacles to avoid the collision between the body and the obstacle, which is called the blue obstacle avoidance control strategy and it is the third priority.

The area between the yellow line and the blue line is the Yellow-Window, which is used to determine the next driving direction of the robot and is called the yellow control strategy. The Yellow Window should be large enough to prevent the robot from driving into such "dead end" areas. The lidar points in the window corresponds to the control strategy of normal steering of the robot: that is, according to the distribution of obstacles, to find the gap with sufficient width for the robot to pass through, and calculate the corresponding steering angles of front and rear wheels. This is the lowest priority.

Each window is further divided into 0-9 small zones, as shown in Figure 13. The robot will decide which obstacle avoidance measure to take according to the distribution of lidar points in each window-zone.

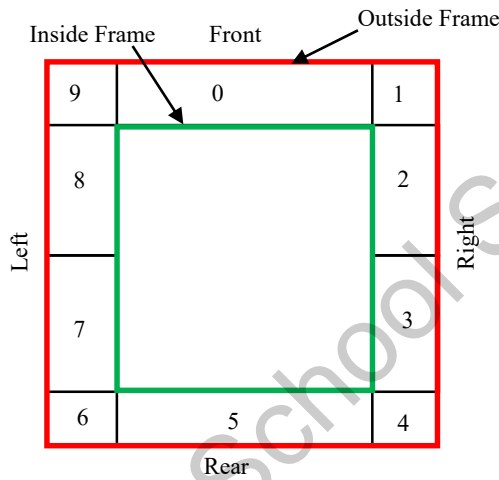


FIGURE 13: The distribution of 10 small zones

4.2 The Yellow-Window Obstacle Avoidance Strategy: Gap-Seeking Theory

When the lidar point is located in the Yellow-window-zone, there will be no emergency collision between the robot and the obstacles. The control system adopts a normal obstacle avoidance control strategy in Figure 14. According to the driving direction, the robot judges the position relationship of the lidar points in the relevant zone. For example, when robot is moving forward, the lidar points in the yellow-window-zone 0, 1, 2, 3, 7, 8, and 9 are determined; Or when backing up, determine the lidar points in zone 2, 3, 4, 5, 6, 7, and 8 of the Yellow-window.

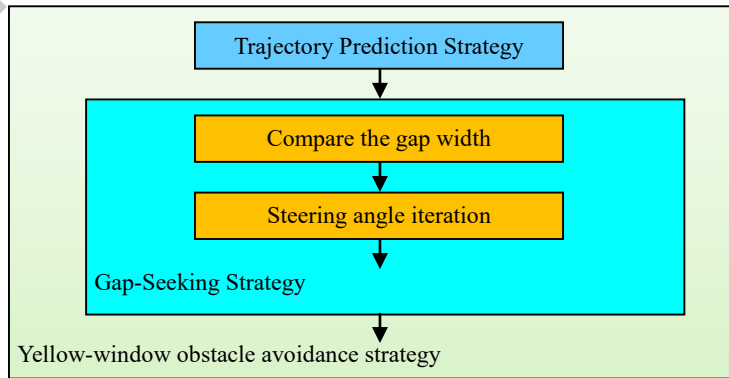


FIGURE 14: Yellow-window obstacle avoidance strategy

4.2.1 Trajectory Prediction Strategy

When the robot is steering, according to Ackerman's theorem, all wheels are controlled to turn around the same steering instantaneous center. Based on this principle, we can calculate the steering moving trajectory circle of each wheel and get the change direction of the trajectory according to the moving direction.

When the robot is running, the trajectories of the wheels of the 2nd, 3rd, and 4th axles are all enveloped between the trajectory of the first and fifth axles. Therefore, only the trajectories of the first and fifth axles are needed to be calculated for predicting the whole robot's moving trajectory. In this way, the calculation model of the whole multi-axle robot's driving trajectories is simplified to the model of the two-axle robot, which greatly reduces the calculation work. This is shown in Figure 15.

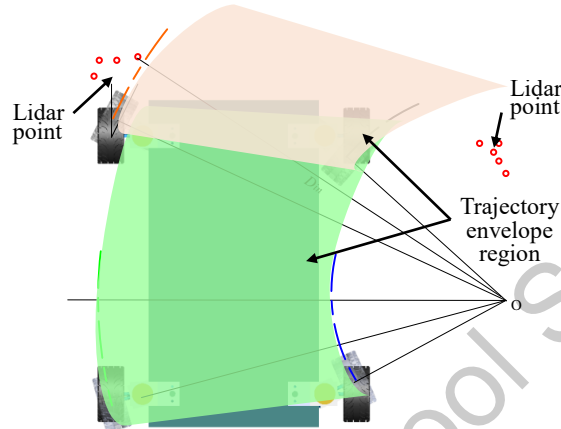


FIGURE 15. The envelope region formed by the trajectory line.

There are 5 steering modes for robots, corresponding to 5 steering trajectory calculation strategies. The trajectory line of the most typical first steering mode is analyzed.

According to equation (4), the wheels' steering angles α_{11} , α_{12} , α_{51} , and α_{52} can be obtained. The angle unit is rad.

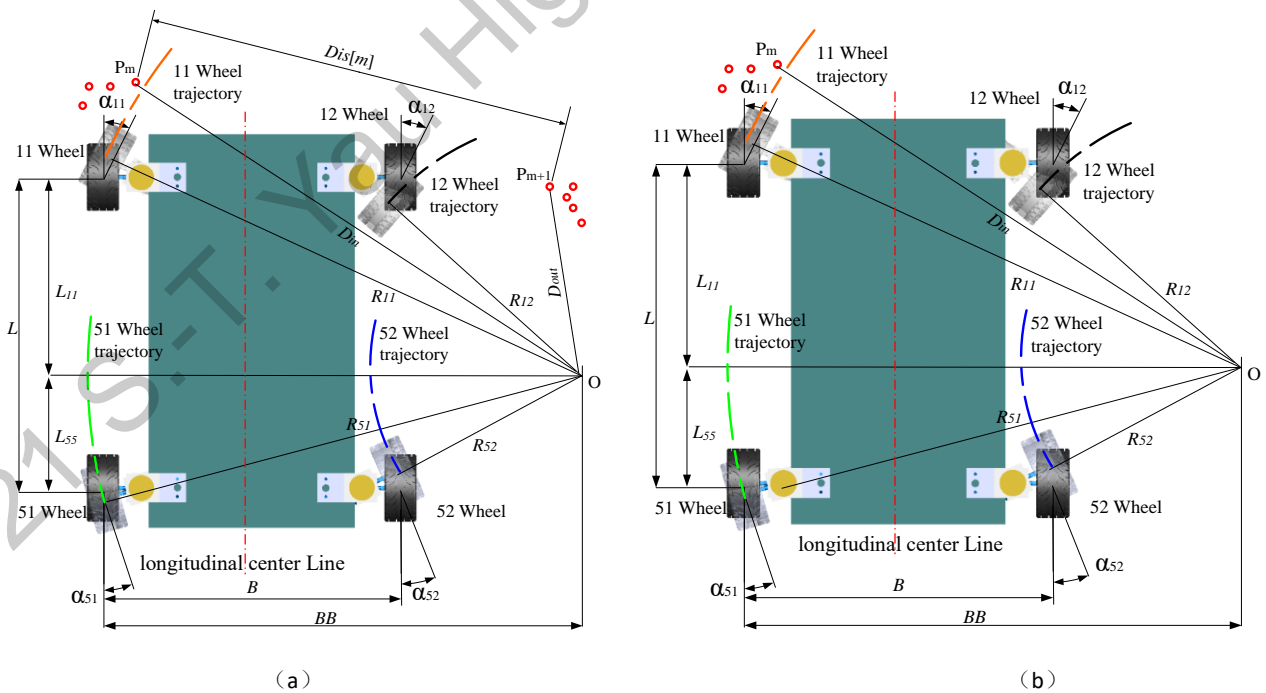


FIGURE 16. Obstacle avoidance geometric relation analysis diagram: (a) The gap has two end points, P_m and P_{m+1} . (b) The gap has only one point P_m .

Longitudinal distance between the robot turning center O and front wheel is (in mm):

$$L_{11} = L \tan(\alpha_{12}) / (\tan(\alpha_{12}) - \tan(\alpha_{52})) \quad (14)$$

Longitudinal distance from center O to the rear wheels is (in mm):

$$L_{55} = L \tan(\alpha_{52}) / (\tan(\alpha_{52}) - \tan(\alpha_{12})) \quad (15)$$

Lateral distance from center O to the left wheel of the 1st axle is (in mm):

$$BB = L_{11} / \tan(\alpha_{12}) \quad (16)$$

Coordinates of the turning center point O are:

$$\begin{aligned} X_C &= xw_{11} + BB \\ Y_C &= yw_{11} - L_{11} \end{aligned} \quad (17)$$

Where xw_{11} , yw_{11} are the x-coordinate and the y-coordinate of the left wheel of the 1st axle, respectively.

According to equations (4), (14)-(17), the coordinates of the k th point in the body's corner point trajectory curves corresponding to the j th wheel in the i th axle in Figure 16 can be obtained as follows:

$$\begin{aligned} XCC_{1j}[k] &= X_C - \text{sign}(\alpha_{12}) R_{1j} \cos(\text{abs}(\alpha_{1j}) + k\Delta\theta) + \Delta Lx_{1j} \\ XCC_{5j}[k] &= X_C - \text{sign}(\alpha_{12}) R_{5j} \cos(\text{abs}(\alpha_{5j}) - k\Delta\theta) + \Delta Lx_{5j} \\ YCC_{1j}[k] &= Y_C + R_{1j} \sin(\text{abs}(\alpha_{1j}) - k\Delta\theta) + \Delta Ly_{1j} \\ YCC_{5j}[k] &= Y_C - R_{5j} \sin(\text{abs}(\alpha_{5j}) + k\Delta\theta) + \Delta Ly_{5j} \\ \Delta\theta &= \pi/180 \\ j &= 1,2 \\ k &= 1,2, \dots, 30 \end{aligned} \quad (18)$$

Where ΔLx_{ij} , ΔLy_{ij} are the compensation distance between four body's corner points and the corresponding four wheels in x and y axis, respectively. $\Delta\theta$ is the iterative step size of the steering angle α_{12} and α_{52} .

4.2.2 Gap-Seeking Strategy

If there are no lidar points in the area enveloped by the steering track lines of each wheel of the robot as shown in Figure 15, it means that the robot can pass the current obstacle with this steering scheme, and it is a feasible steering scheme. Therefore, after the trajectory lines corresponding to the steering angles AF and AR are iteratively calculated and the relationship between the lidar points and the trajectory envelope region is calculated, if the lidar points are all outside the envelope region, then the obstacle avoidance steering scheme is feasible at this time. At this time, AF , AR , and V (the speed of the robot) are the obstacle avoidance control scheme for the next running of the robot.

Since the steering angles of other wheels of the robot are all calculated according to the right front and right rear wheels' steering angles AF and AR , it only needs to calculate AF , AR and speed V in the analysis of obstacle avoidance control. The steering angle of the remaining wheels can be calculated by the robot on-board control unit ESP32S according to the algorithm of the multi-mode steering control strategy.

When the robot moves forward, as shown in Figure 16, the gap-seeking theory is as follows:

1) Compare the gap width $Dis[m]$ and the size of the body width B , and preliminarily select the feasible gap.

First of all, from the obstacle lidar points at the front, left and right sides, gaps that meet the following driving conditions are found.

If the gap has two lidar points, as shown in Figure 16(a), the gap width $Dis[m]$ between two adjacent lidar points P_m and P_{m+1} is compared with the size of the body width B . If $Dis[m] < B$, it indicates that the robot cannot go between two lidar points, so the gap is discarded. Then the gap between the next set of adjacent lidar points is compared. Otherwise, it means that the robot may go between the two lidar points, which is the possible gap. Therefore, the program can continue to run step 2) below.

If the gap has only one lidar point, as shown in Figure 16(b), it goes directly to the step 2) below. The flow chart of comparing the gap width strategy is shown in Figure 17.

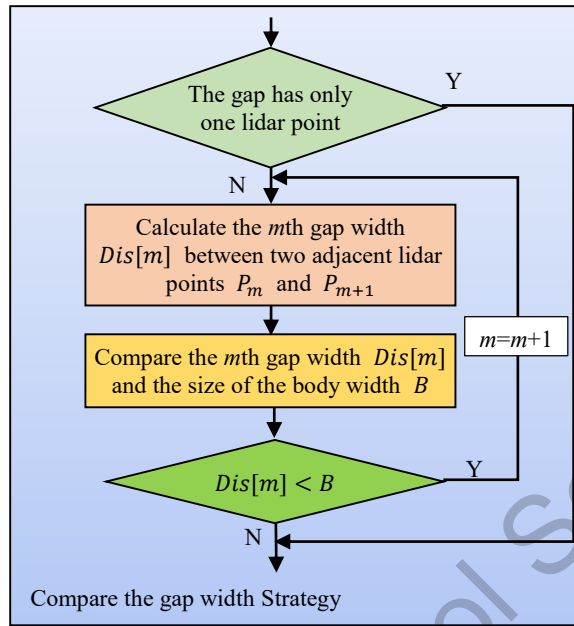


FIGURE 17: Flow chart of comparing the gap width strategy

2) Steering angle iteration

When the robot adopts adverse-phase steering, that is, when the front and rear wheels turn in opposite direction, the turning radius is smaller. In particular, when $AF = -AR$, the turning radius is the smallest. In this case, according to equations (1) - (4) and robot structural parameters in Table 1, the curve of each wheel steering angle changing with virtual front and rear wheels angles can be obtained, as shown in Figure 18. As can be seen from the figure, when $AF = -AR = \pm 65^\circ$, the steering angle curves of some wheels begin to turn, which cannot satisfy all wheels to rotate around the same instantaneous center. Therefore, the variation range of AF should be set as $-65 \sim 65^\circ$. The corresponding range of wheel 11, 12, 51, and 52 for the first axle and fifth axle can be calculated. For example, the variation range of wheel 12 is $-47 \sim 90^\circ$, and that of wheel 52 is $-90 \sim 47^\circ$. In the actual test, we found that the response of steering servo was very accurate and reliable within $\pm 60^\circ$ due to the influence of the installation error of steering servo and the limitation of the control accuracy of steering servo. Therefore, in the actual control, for steering mode 1, we set the steering range of AF and AR as $-60 \sim 60^\circ$ (negative number means counterclockwise steering, positive number means clockwise steering). The value of the ultimate position of each wheel is shown in Table. 2.

Table 1: Geometric parameters of robot. The unit is mm.

The wheelbase of the left and right wheels, B	The distance between 1st and 2nd axles, L_1	The distance between 2nd and 3rd axles, L_2	The distance between 3rd and 4th axles, L_3	The distance between 4th and 5th axles, L_4
230	115	150	117	115

Table 2: The steering angle of four wheels and virtual wheels in the ultimate position. The unit is degree.

	AF or $-AR$	Wheel 11	Wheel 12	Wheel 51	Wheel 52
Theoretical range	65	47	90	-47	-90
	-65	-90	47	90	47
The scope of actual adoption	60	44	84	-44	-84
	-60	-84	-44	84	44

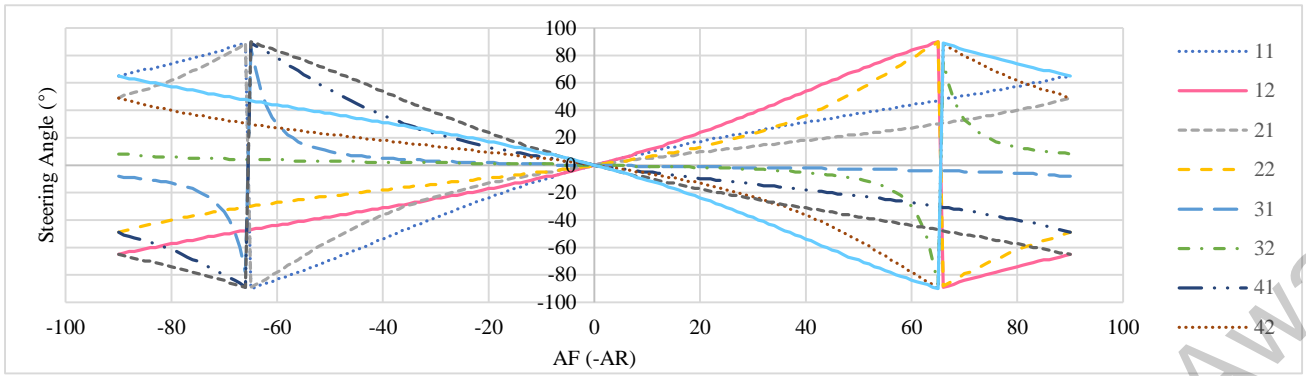


FIGURE 18: Steering angle curves of wheel 11, 12, 21, 22, 31, 32, 41, 42, 51, and 52 changing with front and rear virtual wheels' steering angles when steering mode 1 is adopted. $AF = -AR$.

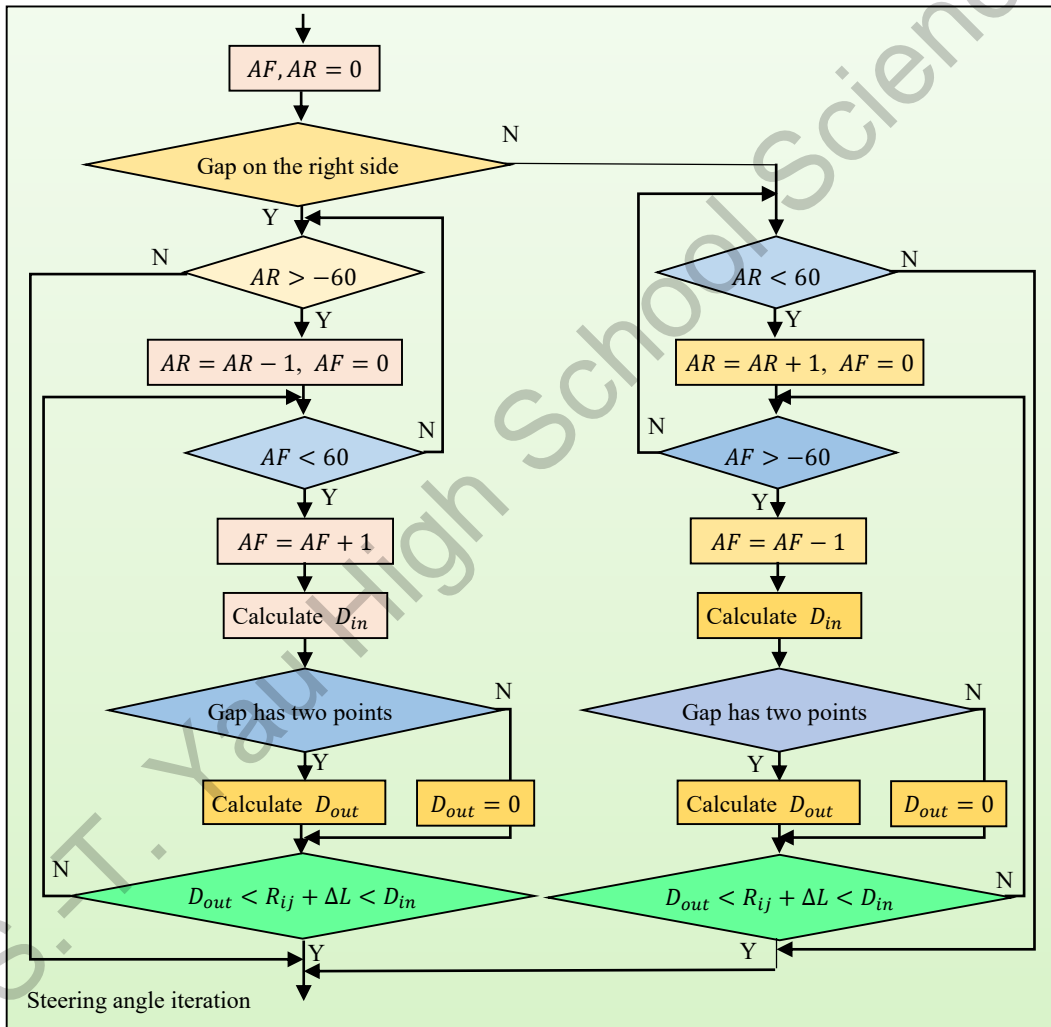


FIGURE 19: Two-level iterative flow chart

The steering angles of the front and rear virtual wheels are iterated in two layers in Figure 19. If the gap is on the right front side, the range of the wheel steering angle is:

$$\begin{aligned} AF &= 0 \sim 60^\circ \\ AR &= -60 \sim 0^\circ \end{aligned} \quad (19)$$

If the gap in the left front side, then the range of the wheel steering angle is:

$$\begin{aligned} AF &= -60 \sim 0^\circ \\ AR &= 0 \sim 60^\circ \end{aligned} \quad (20)$$

According to equations (3), (4),(14)-(18), we can get the coordinates X_C , and Y_C of the turning center point O.

For the lidar points at both sides of the gap, as shown in Figure 16 (a), the one close to the longitudinal center line of the robot body is the inside point, and the one is far away from the longitudinal center line of the robot body is the outside point. Then, the distance between the inside point of the gap and the turning center O is (in mm):

$$D_{in} = \sqrt{(X_C - P_m(x))^2 + (Y_C - P_m(y))^2} - \Delta L \quad (21)$$

Where $P_m(x)$ and $P_m(y)$ are the x and y coordinates of the inside point of the m th gap, respectively. ΔL is the compensation value of the difference between the wheel and the body steering moving trajectory, and the unit is mm.

The calculation of the distance from the outer point of the gap to the turning center O can be divided into two cases:

① Both points of the gap exist, as shown in Figure 16 (a) :

Distance from the outside point of the gap to the turning center O is (in mm):

$$D_{out} = \sqrt{(X_C - P_{m+1}(x))^2 + (Y_C - P_{m+1}(y))^2} + \Delta L \quad (22)$$

Where $P_{m+1}(x)$ and $P_{m+1}(y)$ are the x and y coordinates of the outside point of the m th gap respectively.

② If the gap has only one point and no lidar point on the other side, as shown in Figure 16 (b), we set:

$$D_{out} = 0 \quad (23)$$

The front and rear wheels steering angles AF and AR are iteratively changed within the specified range of (19) or (20) above, until the gap width is larger than the robot body width, and the inside point of the gap is on the outside of the four track curves and the outside point is within the four track curves, as shown in Figure 16. Then the following conditions are satisfied:

$$D_{out} < R_{ij} + \Delta L < D_{in} \quad (i = 1,5; j = 1,2) \quad (24)$$

The angles of the front and rear virtual steering wheels meeting equation (24) are the steering angles for the robot through the gap.

If there are not front and rear virtual wheels steering angles AF and AR that meet equation (24) in the whole iteration process, it means that the robot cannot go through the current gap, and it needs to continue to look for the gap that the robot can go through within the next lidar point by carrying out step 1) and 2).

4.3 Obstacle Avoidance Strategies in Specific Situations

Under normal circumstances, the steering angle of the robot is limited, so it cannot pass the obstacle situation showed in Figure 20. Based on this, combined with the advantages of multi-mode steering of the robot and according to the distribution of obstacles, the following specific obstacle avoidance strategies are proposed on the basis of the obstacle avoidance strategy in the normal yellow window-zone:

1) There are obstacles in front and on both left and right sides, as shown in Figure 20 (a). The robot moves back.

$$\begin{aligned} AF &= 0 \\ AR &= 0 \\ V &= 90 - (V - 90) \end{aligned} \quad (25)$$

2) There are obstacles ahead, no obstacles on left and right sides.

Based on the minimum steering Angle control principle, the gap closest to the longitudinal center line of the robot is found on the left and right sides of the obstacle in front, which is used as the direction of the next moving. As shown in Figure 20 (b), in the case of $LL < LR$, the left side of the front obstacle is close to the longitudinal center line of the body, then the robot will move to the left.

$$\begin{aligned} AF &= 90 \\ AR &= 90 \end{aligned}$$

$$V = 90 - (V - 90) \quad (26)$$

3) There are obstacles in the front and on the left sides, no obstacles on the right side. The robot moves to the right, its speed remains unchanged, as shown in Figure 20 (c).

$$\begin{aligned} AF &= 90 \\ AR &= 90 \\ V &= 90 \end{aligned} \quad (27)$$

4) There are obstacles in the front and on the right sides, no obstacles on the left side. The robot moves to the left, as shown in Figure 20 (d).

$$\begin{aligned} AF &= 90 \\ AR &= 90 \\ V &= 90 - (V - 90) \end{aligned} \quad (28)$$

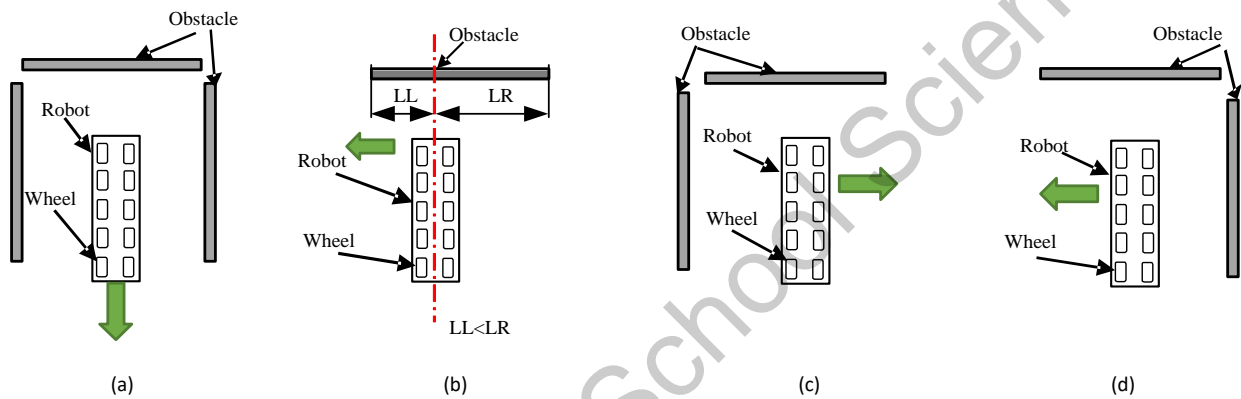


FIGURE 20: Position relation diagram of obstacle and robot. (a) There are obstacles in the front, and on the left and right sides, the robot backs up, (b) There are obstacles in front, no obstacles on the left and right sides. (c) There are obstacles in the front and on the left sides, no obstacles on the right side. (d) There are obstacles in the front and on the right sides, no obstacles on the left side.

5. Control System

The whole control system of the obstacle avoidance robot is mainly composed of software control program and hardware circuit. The software control program is divided into an on-board control system program and upper computer program.

5.1 On-Board Control System Program

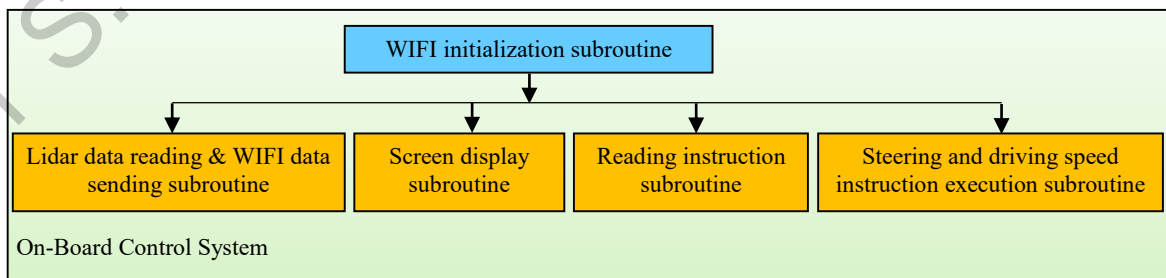


FIGURE 21: On-Board Control System

The program in Figure 21 is used to receive the data from the lidar module, calculate the information of obstacles, and display the relevant information through the touch screen. At the same time, the lidar information is sent to the

upper computer through WIFI, and the robot obstacle avoidance steering and speed control instructions sent by the upper computer are received through WIFI. These instructions are decomposed into the steering angle and wheel speed of 10 wheels. Robot on-board control system procedures include: WIFI initialization subroutine, lidar data reading & WIFI data sending subroutine, touch screen display subroutine, WIFI instruction reading subroutine, steering and driving speed instruction execution subroutine.

1) WIFI INITIALIZATION SUBROUTINE

It is used to set account, password, IP address, port number and so on for WIFI communication, so as to realize wireless data transmission based on WIFI.

2) LIDAR DATA READING & WIFI DATA SENDING SUBROUTINE

It is used to read the information of obstacles produced by lidar through serial communication port and get the angle and distance of obstacle points distribution, and transmit the information to the upper computer through WiFi.

3) ON-BOARD SCREEN DISPLAY SUBROUTINE

It is used to display lidar points data and robot running condition in real-time, and also set up the robot.

4) INSTRUCTION READING SUBROUTINE THROUGH WIFI

This program is used to read the information of steering and speed of the robot for obstacle avoidance sent by the upper computer, detect the status of WIFI communication, and control the robot to stop in time when the WIFI communication is interrupted.

5) STEERING AND DRIVING SPEED INSTRUCTION EXECUTION SUBROUTINE

According to the information received about the speed and steering angles of the front and rear virtual wheels, the steering angles of the ten wheels are calculated with equations (1)-(11).

5.2 Upper Computer Program

The upper computer program in Figure 22 includes a WiFi module, lidar data reading & decomposition module, lidar point selecting & zone division module, obstacle avoidance algorithm module, and travel path prediction-drawing module.

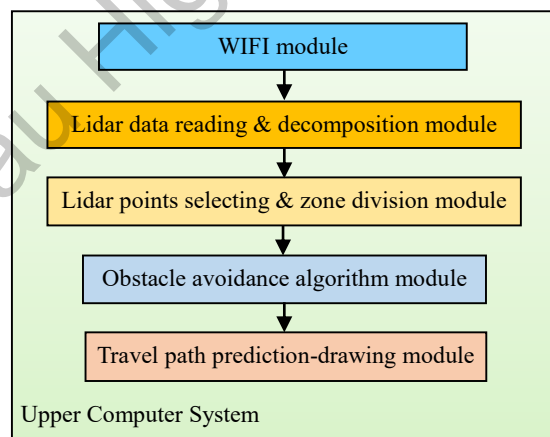


FIGURE 22: Upper Computer System

1) WIFI MODULE

It includes WIFI initialization module, WIFI reading module and WIFI instruction writing module, which is used to complete the wireless communication with the robot on-board control system based on UDP protocol.

2) LIDAR DATA READING & DECOMPOSITION MODULE

According to the communication protocol of the lidar data, the data verification of the lidar points of obstacles and

the calculation of the angle and distance of the lidar points are completed.

3) LIDAR POINTS SELECTING & ZONE DIVISION MODULE

The window-zone control strategy was used to select the lidar points, remove the lidar points in the irrelevant area, and reduce the calculation amount. The distribution of the lidar points in each window-zone was also counted.

4) OBSTACLE AVOIDANCE ALGORITHM MODULE

It mainly includes: window-zone emergency obstacle avoidance module, yellow window-zone gap-seeking normal obstacle avoidance module, and other obstacle avoidance modules.

5) TRAVEL PATH PREDICTION-DRAWING MODULE

This module mainly calculates and draws the robot's next running trajectory according to the steering angle AF , AR of the front and rear virtual wheels, and speed V with equation (18).

6. Experimental Verification

To verify the obstacle avoidance control strategy proposed above, experiments of Z-shaped with different passage widths were carried out as shown in Figure 21-23. To verify the robustness of the obstacle avoidance control strategy proposed, experiments of S-shaped, U-shaped, and random obstacle distribution were carried out, as shown in Figure 24-33. Most of the passage widths among obstacles is smaller than the length of the robot body, it meets the layout requirements of the narrow space. During the whole autonomous driving process, the initial speed threshold of the robot is set to 108, and the actual driving speed is about 256mm/s.

6.1 Z-Shaped Obstacle Distribution

The size of the obstacle distribution is shown in Figure 21. Comparison experiments of 6 passage widths were conducted. The width sizes W_i are 620, 600, 580, 550, and 500 mm, respectively. For each passage width, AWS (All-Wheel-Steering) and NAWS (Non-All-Wheel-Steering, only the last axle does not turn.) obstacle avoidance control strategies were adopted, respectively. The results are shown in Table 3 and Figure 22, 23.



FIGURE. 21: The size of Z-shaped obstacle distribution. The unit is mm.

The passage widths among obstacles in all experiments are all narrower than the length of the robot body, except the first experiment. They meet the layout requirements of the narrow space.

Table 3: Obstacle avoidance experiment results of different passage widths.

The order	Passage width W_i (mm)	AWS	NAWS
1 st	620	Pass	Pass
2 nd	600	Pass	Pass
3 rd	580	Pass	Pass with local collision
4 th	550	Pass	Pass with local collision
5 th	500	Pass with local collision	No pass

When the width of the passage is larger than or equal to the length 600mm of the robot body, both of the two control strategies can control the robot to pass the obstacles smoothly, and achieve the avoid obstacle effect of conventional circular robot body shape. When the passage width is less than the body length, such as 580 or 550mm, both schemes can pass, but local collisions occur with the NAWS scheme. When the passage width is further reduced to 500mm, AWS can pass but local collisions occur and NAWS cannot pass.

According to (a), (c), (e) and (g) in Figure 22, it can be seen that the distance between the track lines of front and rear endpoints A and B of the AWS scheme is smaller than that of NAWS, indicating that AWS takes up less space and is more suitable for obstacle avoidance in a narrow space.

The control output of steering variables AF and AR of the front and rear virtual wheels and speed V is shown in Figure 22 (b), (d), (f), and (h). As can be seen from the figure, as the passage width becomes narrower, the steering angles of the two control schemes are frequently oscillated to adjust the position of the robot for obstacle avoidance. In the AWS scheme, the rear virtual wheel AR appears more fluctuations to adjust the position of the rear part of the robot body for obstacle avoidance. In particular, many adverse-phase steering schemes with front and rear wheels adverse steering are adopted to obtain smaller turning radius and meet the need of obstacle avoidance in narrow space.

Figure 23 is a statistical graph of the time cost of obstacle avoidance calculation in the process of obstacle avoidance test above, based on the distribution of obstacles collected by lidar each time. Passage widths are 620mm, 600mm, 580mm, and 550mm, respectively. Control strategy is NAWS and AWS. Time range is ‘lower than 10ms’, ‘between 10 and 20ms’, and ‘larger than 20ms’, respectively. Figure 23 (a) is the statistics of the times of obstacle avoidance, and Figure 23 (b) is the percentage of the times in the corresponding period to the total times in the whole process of obstacle avoidance. The specific calculation equation is

$$P_i = \frac{N_i}{N} \times 100\% \quad (28)$$

P_i is the percentage of the number of obstacle avoidance computations in the corresponding i th period of time to the total number of obstacle avoidance computations in the entire obstacle avoidance process. N_i is the number of times in the period T_i of the obstacle avoidance calculation cost. The time periods are

$$\begin{aligned} T_i &\leq 10 \text{ ms} \\ 10 &< T_i < 20 \text{ ms} \\ T_i &\geq 20 \text{ ms} \end{aligned} \quad (29)$$

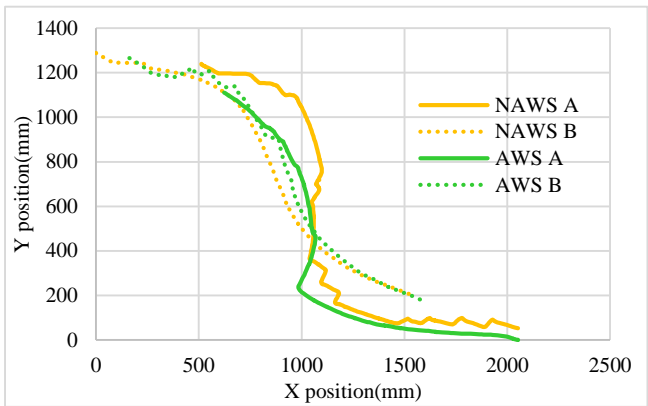
N is the total number of obstacle avoidance calculations in the whole obstacle avoidance test.

As can be seen from the Figure 23, in all experiments, for the obstacle avoidance algorithm proposed in this paper, the times of obstacle avoidance calculation time overhead above 20ms are all less than 4%. In other words, in the whole process of obstacle avoidance, for the obstacle information collected by lidar each time, the calculation time of the obstacle avoidance algorithm is much lower than the lidar scanning time of 100ms. These cases are up to 96% in the total number of obstacle avoidance counts. It shows that the time response of this algorithm is very fast and meets the requirement of real-time obstacle avoidance. In addition, as the width of the passage narrows, the percentage of each obstacle avoidance calculation time less than 10ms becomes smaller during the entire obstacle avoidance process. This indicates that the narrower the passage, the larger the steering angle, and the more iterations. As a result, for each obstacle distribution information collected by lidar, the corresponding obstacle avoidance

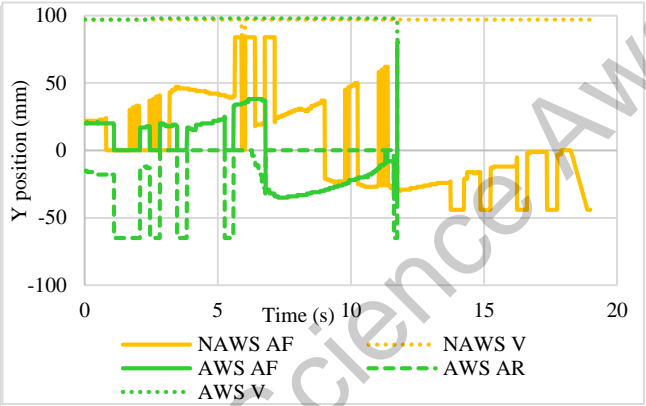
calculation time is more.

Because only the single-layer iterative obstacle avoidance calculation of NAWS mode is used, the overall time cost of NAWS mode is shorter than that of the double-layer iterative model of the front and rear wheels in AWS mode.

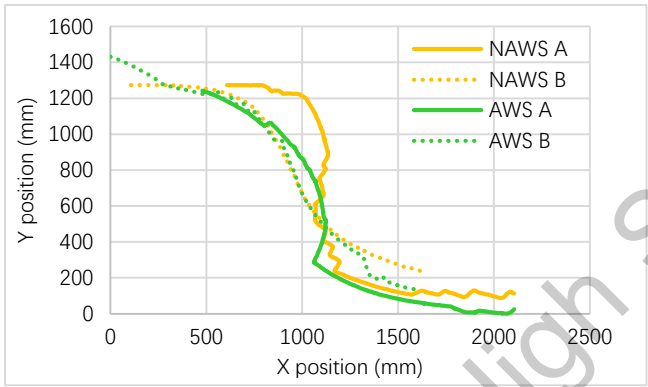
The above experimental results show that the proposed obstacle avoidance control strategy is better than the traditional obstacle avoidance control strategy of circular robot, and can pass through the passage less than the body length, and AWS scheme is better than NAWS, and can pass through a narrower area.



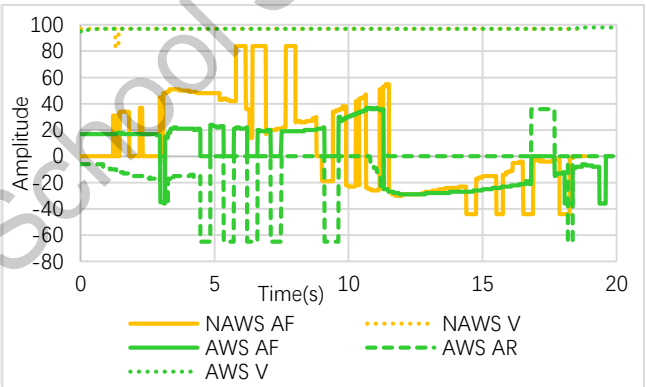
(a)



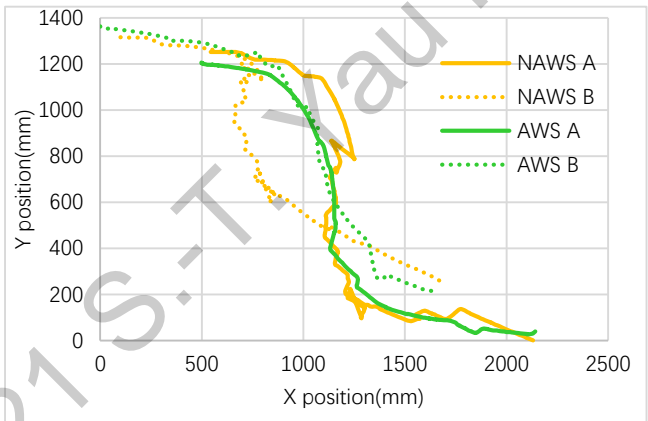
(b)



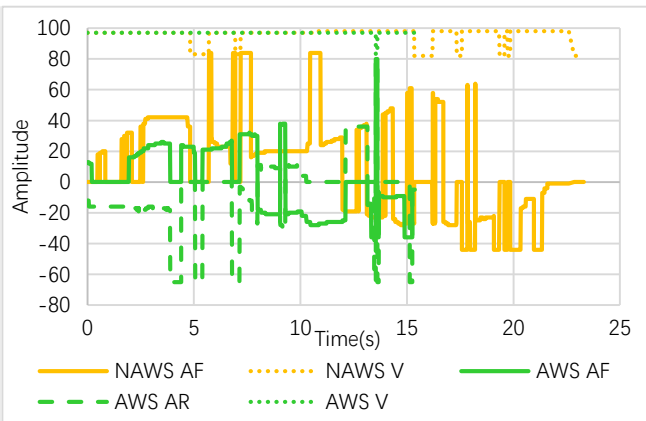
(c)



(d)



(e)



(f)

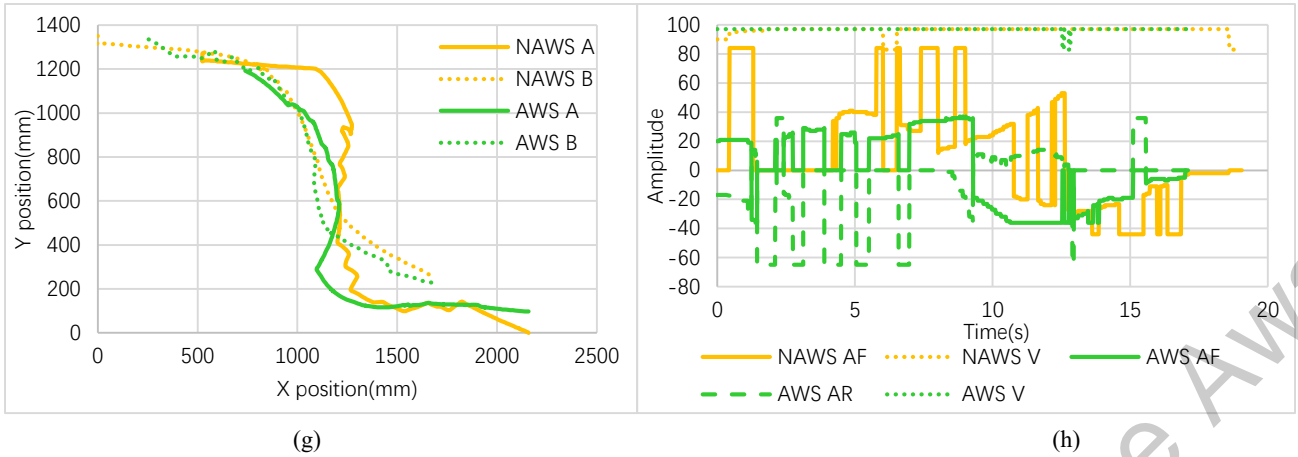


FIGURE 22. Z-shaped obstacle distribution experiment. The position of A and B is shown in Figure 2. NAWS A and NAWS B are trajectory curves of head point A and rear point B of the body, respectively, and the strategy is NAWS. AWS A and AWS B are trajectory curves of head point A and rear point B of the body, respectively, and the strategy is AWS. NAWS AF and NAWS V are front wheel steering angle (The unit is degree), and speed control variable, respectively, and the strategy is NAWS. AWS AF, AWS AR, and AWS V are front and rear virtual wheels steering angle, and speed control variable, respectively, and the strategy is AWS.

(a) Trajectory curves of head point A and rear point B of the body. The passage width is 620 mm. (b) Steering angle of *AF* & *AR*, and speed control variable *V*. The passage width is 620 mm. (c) Trajectory curves of head point A and rear point B of the body, and The passage width is 600 mm. (d) Steering angle of *AF* & *AR*, and speed control variable *V*. The passage width is 600 mm. (e) Trajectory curves of head point A and rear point B of the body. The passage width is 580 mm. (f) Steering angle of *AF* & *AR*, and speed control variable *V*. The passage width is 580 mm. (g) Trajectory curves of head point A and rear point B of the body. The passage width is 550 mm. (h) Steering angle of *AF* & *AR*, and speed control variable *V*. The passage width is 550 mm.

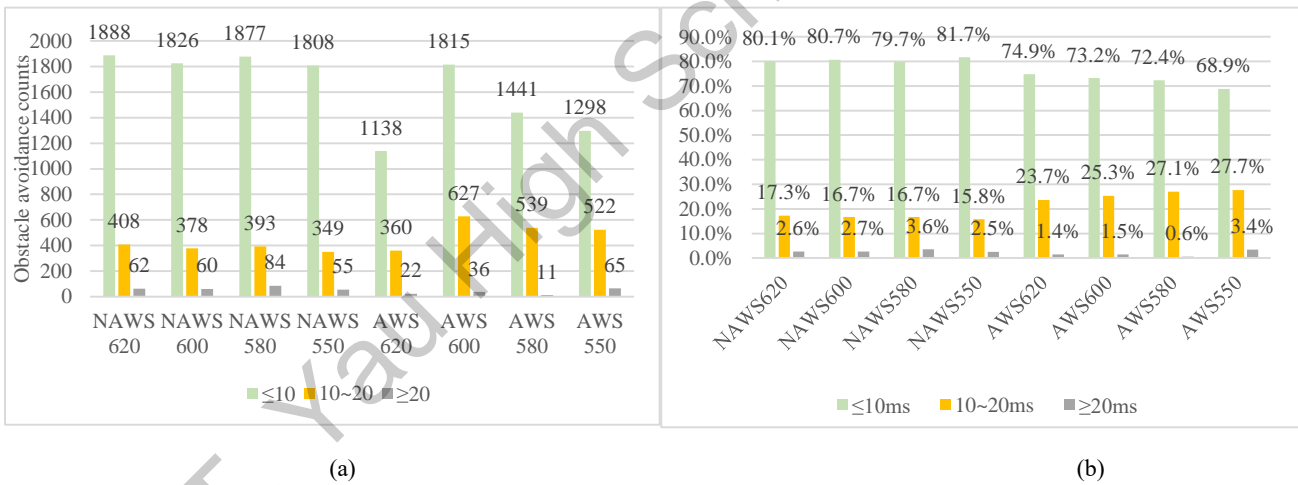


FIGURE 23: The time cost for obstacle avoidance. The passage widths are 620mm, 600mm, 580mm and 550mm, respectively. The control strategies are AWS and NAWS. The time period is 'lower than 10ms', 'between 10 and 20ms', and 'larger than 20ms', respectively. (a) Statistics of obstacle avoidance times in each time period of different test schemes; (b) Statistics on the percentage of the number of obstacle avoidance times in each time period of different test schemes to the total number of obstacle avoidance times of this obstacle avoidance test.

6.2 S-Shaped Obstacle Distribution

The S-shaped obstacle avoidance experiments were carried out three times in total, with an area size of 3550mm×1815mm and a passage width of 500~650mm. The control strategy is AWS. The distribution of obstacle passage and experimental results are shown in Figure 24-26.

In the first experiment, as shown in Figure 24(a), the robot entered from the top-right corner of the figure and sailed out of the passage smoothly without hitting any obstacle. The motion tracks of the front and rear marking points A and B (as shown in Figure 2) are shown in Figure 24(a) and (b). The track curves are almost located at the middle

line of the passage, and the obstacle avoidance effect is good. At point C, the obstacle invades into zones 7-8 of the blue window, as shown in Figure 24(d). Thanks to the independent control of the steering of each wheel, the rear of the robot can be corrected for emergency translation in order to avoid collision with obstacles. Thus, the inflection point of the trajectory at C is formed. During the whole running process, the rear of the robot adjusts in real-time according to the position of the head, so the track of point B always swings up and down in the track of point A. Figure 24 (c) shows the curves of the front wheel steering angle AF , rear wheel steering angle AR and speed V of the robot. From these curves, we can see the obstacle avoidance measures taken by the robot according to the information of obstacles collected by the lidar. For example, at 3.2 seconds, both AF and AR are 80° , and the speed V is 71. It indicates that the robot adopts the steering mode of left lateral translation to carry out emergency obstacle avoidance.

In the second experiment, the robot still entered from the top-right corner of the figure, but based on Figure 24(a), the angle of obstacles at the yellow circle was reduced from 127.6° to 101.3° , to reduce the width of the channel here and increase the difficulty of obstacle avoidance of S-shaped obstacles, as shown in Figure 25(a). Due to this change, inflection points appear at C and D of trajectory curves of Figure 25(a) and (b). The obstacle at point C invades zone 9 of the blue window, and the robot takes the obstacle avoidance measure of emergency right turn of the head, as shown in Figure 25(c) and (d). The obstacle at D invades the 0 and 1 zone of the blue window, and the robot takes the obstacle avoidance measure backward to the left, as shown in Figure 25(c) and (e). The robot can go through the channel smoothly throughout the process.

The third experiment is shown in Figure 26(a). The distribution of obstacles is the same as that in Figure 25(a), but the robot enters from the bottom-left corner of the figure, and the corresponding traveling trajectory curves at the yellow circle change dramatically. At this time, the lidar in Figure 26(d) shows that obstacles invade the blue window 0-1 zone and yellow window 7-8 zone, and the robot transverses to the left to avoid obstacles and urgently adjusts the body away from the obstacle on the right to realize the obstacle avoidance strategy with small space occupied so that the trajectory at C appeared in Figure 26(b) is shifted. At this time, AF and AR are both 80° and the speed V is 71, as shown in Figure 26(c).

Through experiments, it is proved that the proposed control strategy can achieve successfully multi-mode autonomous obstacle avoidance in a narrow space of S-shaped obstacle.

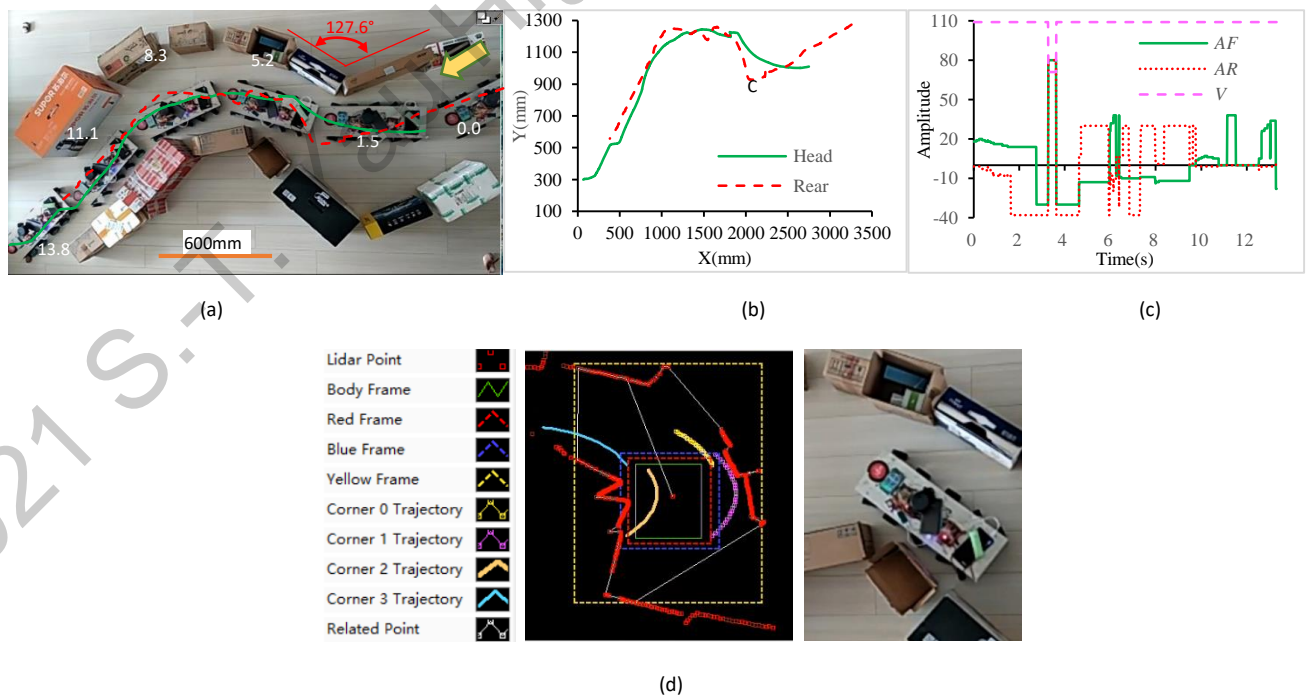


FIGURE 24: 1st S-shaped obstacle distribution experiment. (a) Robot trajectory diagram of S-shaped obstacle avoidance. (b) Trajectory curves of head point A and rear point B of the body, and the position of A and B is shown in Figure 2. (c) Steering angles of AF & AR

(The unit is degree), and speed control variable V . (d) When the robot moves to point C, the lidar map (The head of the robot is always upward in the figure) and the corresponding actual obstacle distribution map (The head of the robot is facing up to the left in the figure).

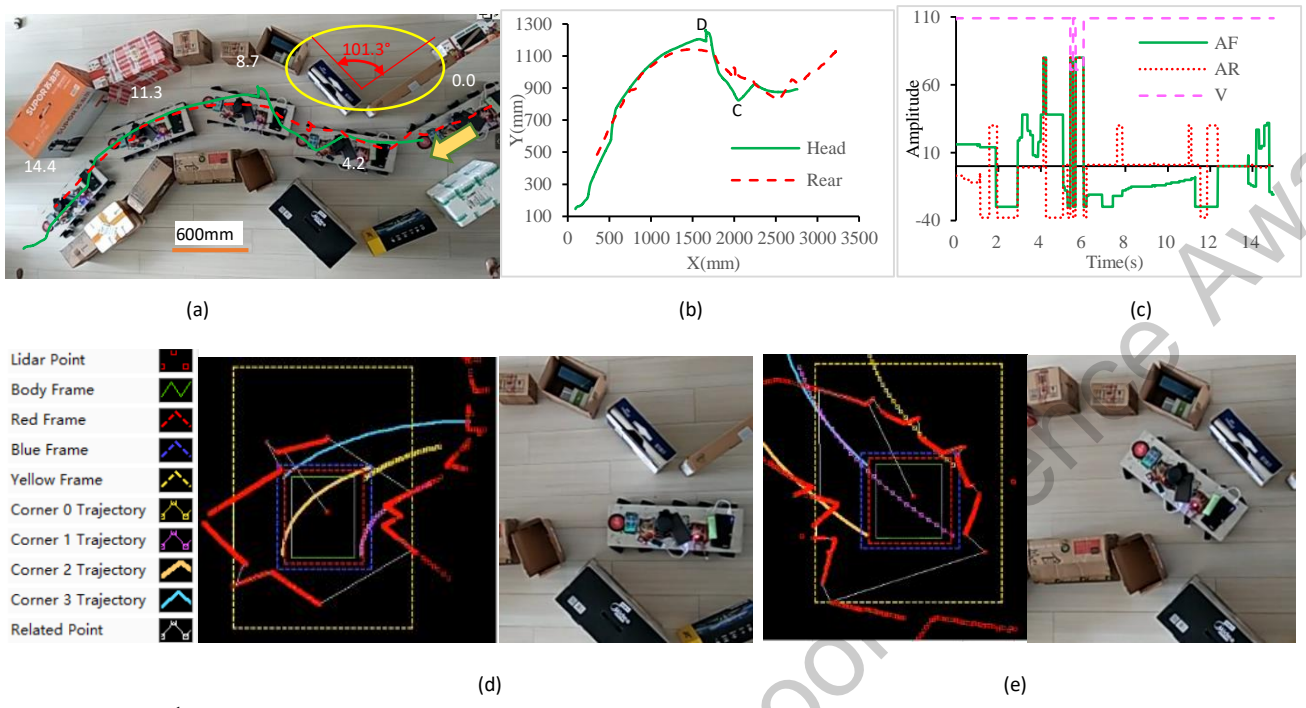


FIGURE 25: 2nd S-shaped obstacle distribution experiment. (a) Robot trajectory diagram of obstacle avoidance. (b) Trajectory curves of head point A and rear point B of the body, and the position of A and B is shown in Figure 2. (c) Steering angles of AF & AR (The unit is degree), and speed control variable V . (d) When the robot moves to point C, the lidar map (The head of the robot is always upward in the figure) and the corresponding actual obstacle distribution map (the head of the robot towards left in the figure). (e) When the robot moves to point D, the lidar map (the head of the robot is always up in the figure) and the corresponding actual obstacle distribution map (The head of the robot is facing up to the left in the figure).

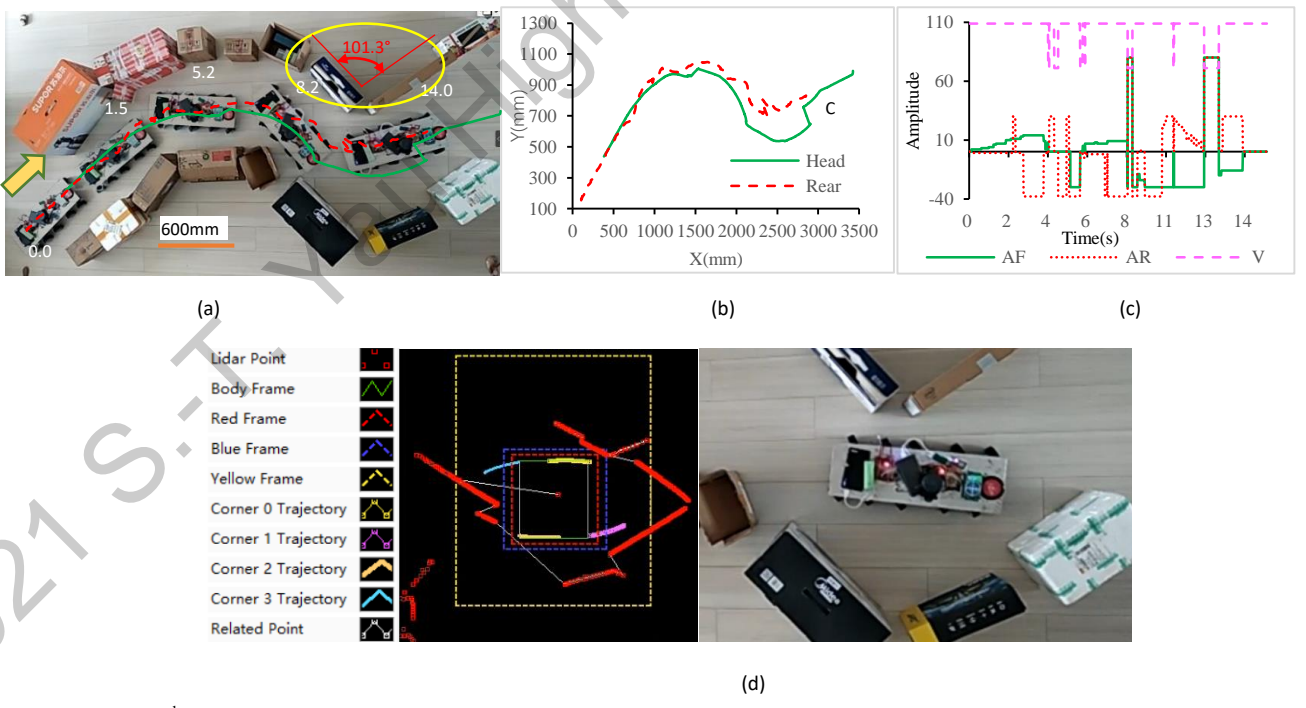


FIGURE 26: 3rd S-shaped obstacle distribution experiment. (a) Robot trajectory diagram of S-shaped obstacle avoidance. (b) Trajectory curves of head point A and rear point B of the body, and the position of A and B is shown in Figure 2. (c) Steering angles of AF & AR (The unit is degree), and speed control variable V . (d) When the robot moves to point C, the lidar map (The head of the robot is always upward in the figure) and the corresponding actual obstacle distribution map (The head of the robot towards right in the figure).

6.3 U-Shaped Obstacle Distribution

The area size is 2160mm×1580mm, and the width of the driving channel is 520~670mm. The control strategy is AWS. The U-shaped obstacle avoidance experiments were carried out 5 times. The robot can all pass autonomously without hitting any obstacle. Two representative experiments were selected for analysis. The distribution of obstacle passage and experimental results are shown in Figure 27-28.

In the first experiment, shown in Figure 27(a), the robot enters from the top-right corner of the figure. At the first corner C, the adverse-phase steering strategy with the front wheel variable AF turning 18° to the right and the rear wheel variable AR turning 38° to the left was adopted to minimize the occupying of obstacle avoidance space, as shown in Figure 27(d). At the second corner D, the adverse-phase steering control strategy with the front wheel variable AF turning 19° to the left and the rear wheel variable AR turning 38° to the right was adopted to realize the flexible steering mode with a small radius, as shown in Figure 27 (e). During the whole running process, the motion trajectory of body points A and B is shown in Figure 27(a) and (b), and the output of steering variables AF and AR of front and rear wheels and speed V is shown in Figure 27(c). Lidar point map and actual obstacle distribution at C and D are shown in Figure 27(d) and (e).

The second experiment is to add an obstacle at the yellow circle in Figure 28 (a) based on Figure 27(a) to reduce the passage space here and increase the difficulty of passing. At the same time, the starting point of the robot is changed to the top-left corner. At D in Figure 28 (b), due to the narrow channel space, the robot adopts an adverse-phase steering control strategy of front wheel control variable AF turning 17° to the left, rear wheel control variable AR turning 30° to the right, and the speed V being 109 to reduce the occupied space of obstacle avoidance. At C, because the obstacle invades the blue window zone 1, the robot adopts the control strategy of left lateral translation with the wheel steering control variable AF and AR of 80° and the speed V of 71 to avoid the obstacle on the right. During the whole driving process, the motion trajectory of body points A and B is shown in Figure 28(a) and (b), and the control output of steering variables AF and AR of front and rear wheels and speed V is shown in Figure 28(c). Lidar point map and actual obstacle distribution at C and D are shown in Figure 28(d) and (e).

Through avoidance experiments, it is proved that the designed control strategy can realize successfully the multi-mode autonomous obstacle avoidance in the narrow space of U-shaped obstacle.

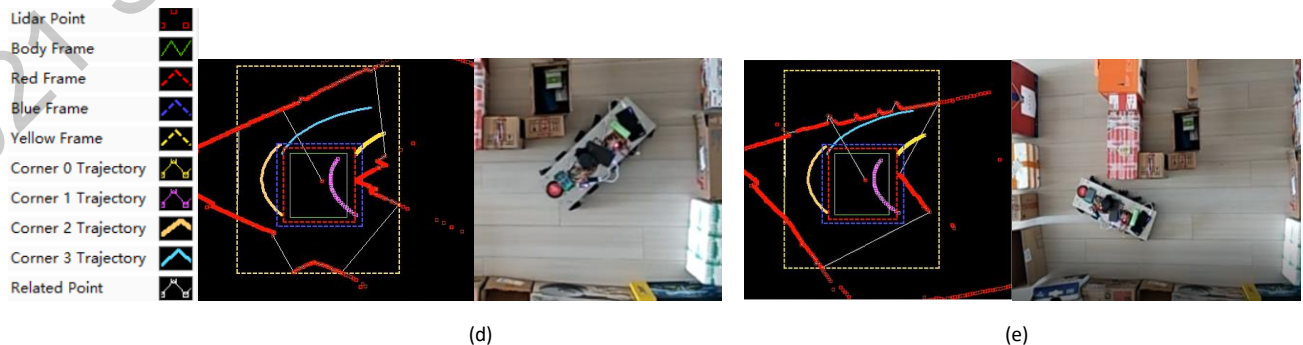
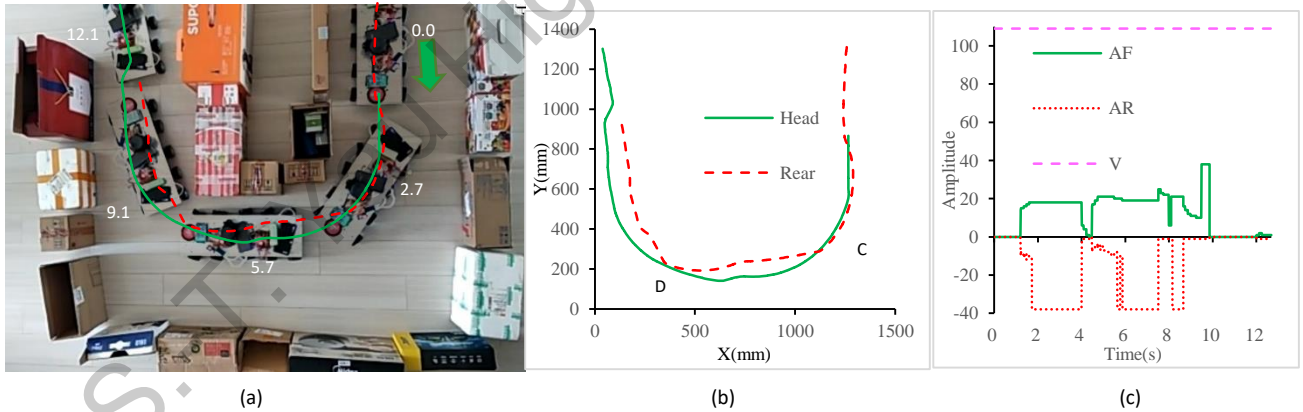


FIGURE 27: 1st U-shaped obstacle distribution experiment. (a) Robot trajectory diagram of U-shaped obstacle avoidance. (b)

Trajectory curves of head point A and rear point B of the body, and the position of A and B is shown in Figure 2. (c) Steering angles of AF & AR (The unit is degree), and speed control variable V . (d)When the robot moves to the first corner C, the lidar map (The head of the robot is always upward in the figure) and the corresponding actual obstacle distribution map (The head of the robot is facing down to the left in the figure). (e)When the robot moves to the second corner D, the lidar map (The head of the robot is always upward in the figure) and the corresponding actual obstacle distribution map (The head of the robot is facing up to the left in the figure).

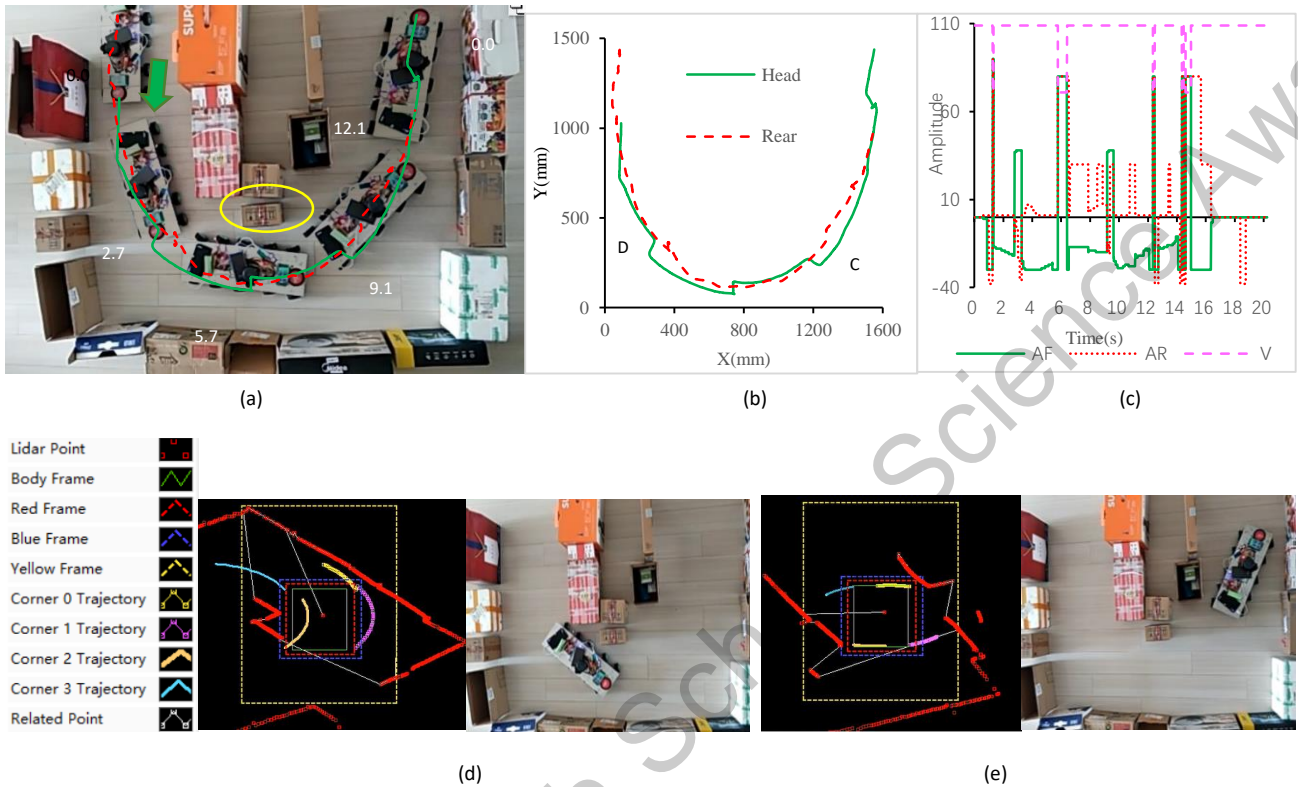


FIGURE 28: 2nd U-shaped obstacle distribution experiment. (a) Robot trajectory diagram of U-shaped obstacle avoidance. (b) Trajectory curves of head point A and rear point B of the body, and the position of A and B is shown in Figure 2. (c) Steering angles of AF & AR (The unit is degree), and speed control variable V . (d)When the robot moves to the second corner D, the lidar map (The head of the robot is always upward in the figure) and the corresponding actual obstacle distribution map (The head of the robot is facing down to the right in the figure). (e)When the robot moves to the first corner C, the lidar map (The head of the robot is always upward in the figure) and the corresponding actual obstacle distribution map (The head of the robot is facing up to the right in the figure).

6.4 Random Obstacle Distribution

Six obstacle avoidance experiments with a random distribution of obstacles were designed, and the area size is 2920mm×1500mm. The control strategy is AWS. In all the experiments, the robot can pass autonomously without colliding with obstacles. Five representative experiments were selected for analysis. The distribution of obstacle and experimental results are shown in Figure 29-33.

The distribution of obstacles in the first experiment is shown in Figure 29(a). The robot enters from the left side of the figure. As the channel curve changes rapidly, the obstacle at C incurs into the blue window zone 1, as shown in Figure 29(d). Therefore, the robot adopts the control strategy of moving to the left and back side with the front wheel control variable AF and AR of 80° and the speed V of 71 to avoid the right front obstacle, so that the trajectory curve in Figure 29(a) and (b) appears lateral shifting. Control outputs of front and rear wheels steering variables AF , AR and speed V are shown in Figure 29(c).

The obstacle distribution of the second experiment is shown in Figure 30(a). The purpose of the second experiment is to verify the nearby selection strategy of the robot for multiple gaps. The robot enters from the bottom-left of the figure. It can be seen that in the case of multiple gaps, the robot chooses the gap with small steering angle preferentially, so the robot keeps almost running in a straight line. At D of Figure 30(b), obstacles invade blue window zones 0 and 2, and red window zone 1 as shown in Figure 30(d). Therefore, the robot adopts the control strategy of

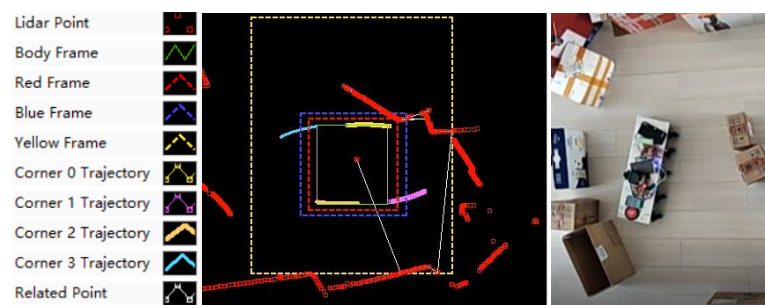
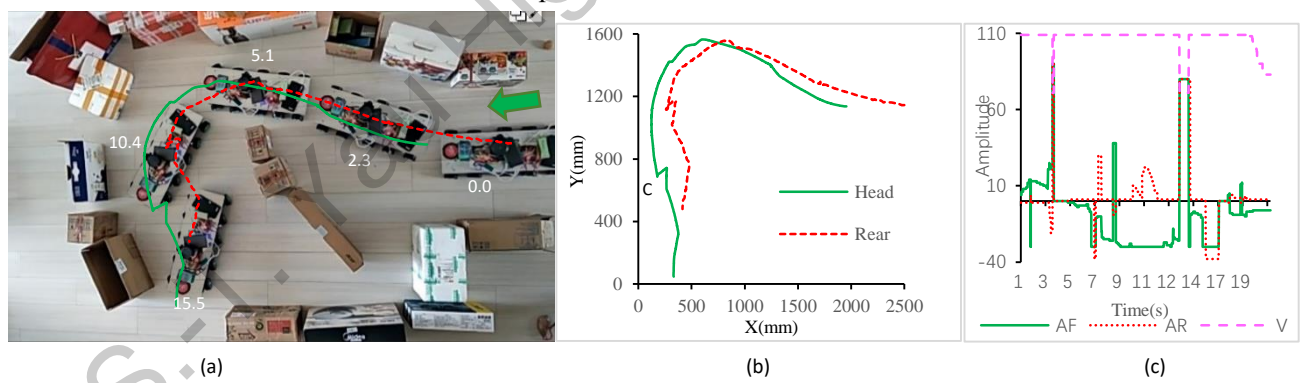
moving to the left and back side with the front wheel control variable AF and AR of 80° and the speed V of 71 to avoid the right front obstacle, so the trajectory curve at D in Figure 30(a) (b) appears lateral shifting. At C of Figure 30(b), obstacles invade zones 1 and 2 of the blue window, as shown in Figure 30(e). Therefore, the robot adopts a control strategy of the front wheel control variable AF turning to the left at 30° , the rear wheel control variable AR turning to the left at 38° , and the speed V is 109, so as to avoid the obstacles on the right front, so the trajectory curve at C in Figure 30(a) (b) appears a lateral shift. Outputs of front and rear wheels steering variables AF , AR and speed V are shown in Figure 30(c).

The distribution of obstacles in the third experiment is shown in Figure 31(a), which aims to verify the nearby selection strategy of the robot for multiple gaps. The robot enters from the right side of the figure. As can be seen from the figure, in the case of multiple gaps, the robot preferred the gap with small steering angles, so the robot basically kept running in a straight line. The trajectory curve is shown in Figure 31(a) and (b). Control outputs of front and rear wheels steering variables AF , AR and speed V are shown in Figure 31(c).

The obstacle distribution in the fourth experiment is the same as that in the third experiment, as shown in Figure 32(a). However, the robot entered from the left side of the figure, and the initial body position of the robot was adjusted to tilt downward at a certain angle. As can be seen from Figure 32(b), in the case of multiple gaps in the CD track curves, the robot gives priority to the gaps with small steering angles, so the robot keeps almost running in a straight line along the direction of the robot body. Control outputs of front and rear wheels steering variables AF , AR and speed V are shown in Figure 32(c).

The distribution of obstacles in the fifth experiment is shown in Figure 33(a). Based on Figure 32(a), an obstacle is added to the yellow circle in Figure 33(a) to reduce the passage space here, change the curve shape of the passage, and increase the difficulty of obstacle avoidance. The robot enters from the right side of the figure. It can be seen from Figure 33 (b), the trajectory curves change sharply, indicating that the robot can adapt to sharp channel changes and realize sharp turn to avoid obstacles. It can be seen from Figure 33 (c), the robot repeatedly moved to the left and back with the wheel control variables AF and AR of 80° and the speed V of 71. In this way, it can avoid obstacles on the right side and adjust the body posture to pass through the channel with drastic change.

Through the experiments, it is proved that the proposed control strategy can realize successfully the multi-mode autonomous obstacle avoidance in the narrow space of random obstacle distribution.



(d)

FIGURE 29: 1st Random obstacle distribution experiment. (a) Robot trajectory diagram of random obstacle avoidance. (b) Trajectory curves of head point A and rear point B of the body, and the position of A and B is shown in Figure 2. (c) Steering angles of AF & AR (The unit is degree), and speed control variable V . (d) When the robot moves to point C, the lidar map (The head of the robot is always upward in the figure) and the corresponding actual obstacle distribution map (The head of the robot is facing down to the left in the figure).

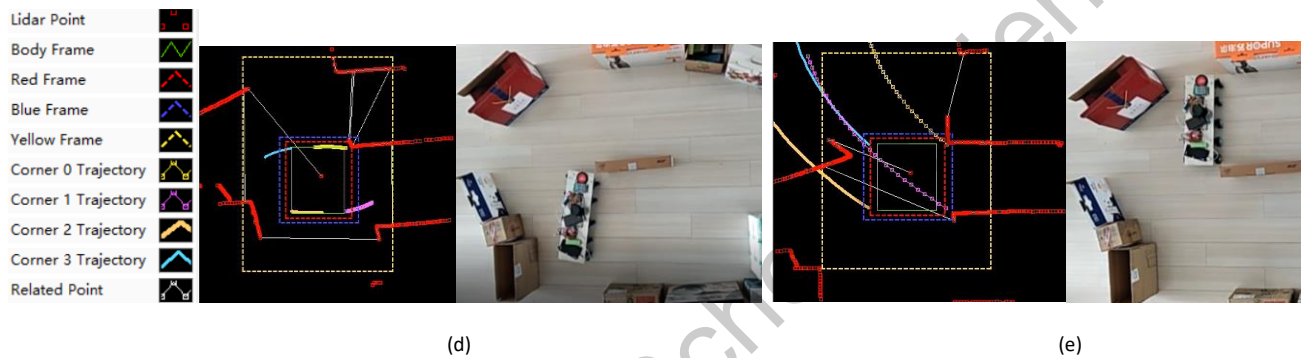
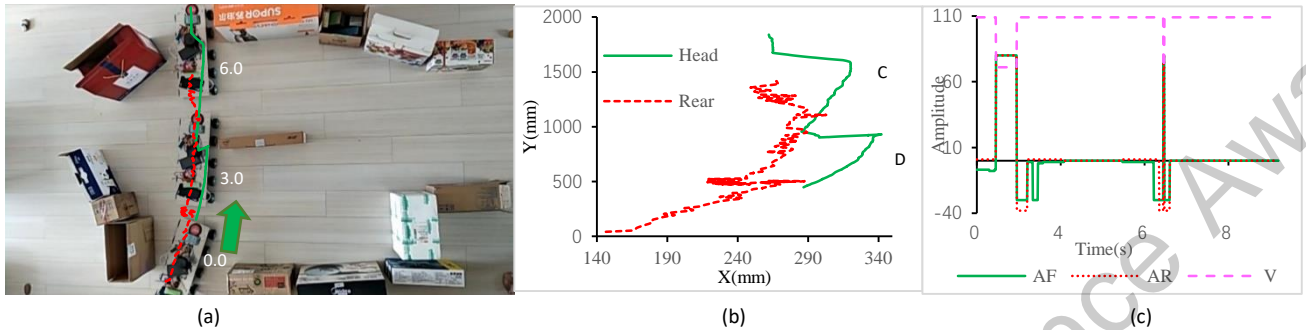


FIGURE 30: 2nd Random obstacle distribution experiment. (a) Robot trajectory diagram of random obstacle avoidance. (b) Trajectory curves of head point A and rear point B of the body, and the position of A and B is shown in Figure 2. (c) Steering angles of AF & AR (The unit is degree), and speed control variable V . (d) When the robot moves to point D, the lidar map (The head of the robot is always upward in the figure) and the corresponding actual obstacle distribution map (the head of the robot is upward in the figure). (e) When the robot moves to point C, the lidar map (The head of the robot is always upward in the figure) and the corresponding actual obstacle distribution map (The head of the robot is upward in the figure).

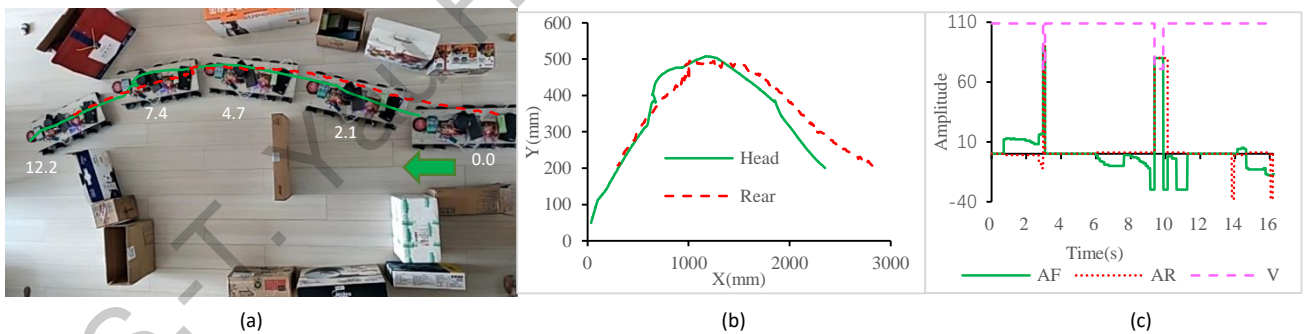


FIGURE 31: 3rd Random obstacle distribution experiment. (a) Robot trajectory diagram of random obstacle avoidance. (b) Trajectory curves of head point A and rear point B of the body, and the position of A and B is shown in Figure 2. (c) Steering angles of AF & AR (The unit is degree), and speed control variable V .

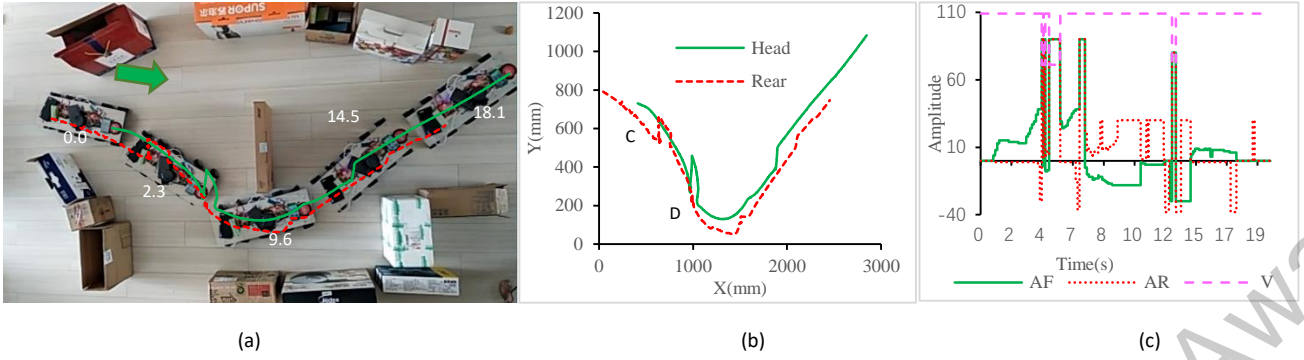


FIGURE 32: 4th Random obstacle distribution experiment. (a) Robot trajectory diagram of random obstacle avoidance. (b) Trajectory curves of head point A and rear point B of the body, and the position of A and B is shown in Figure 2. (c) Steering angles of *AF* & *AR* (The unit is degree), and speed control variable *V*.

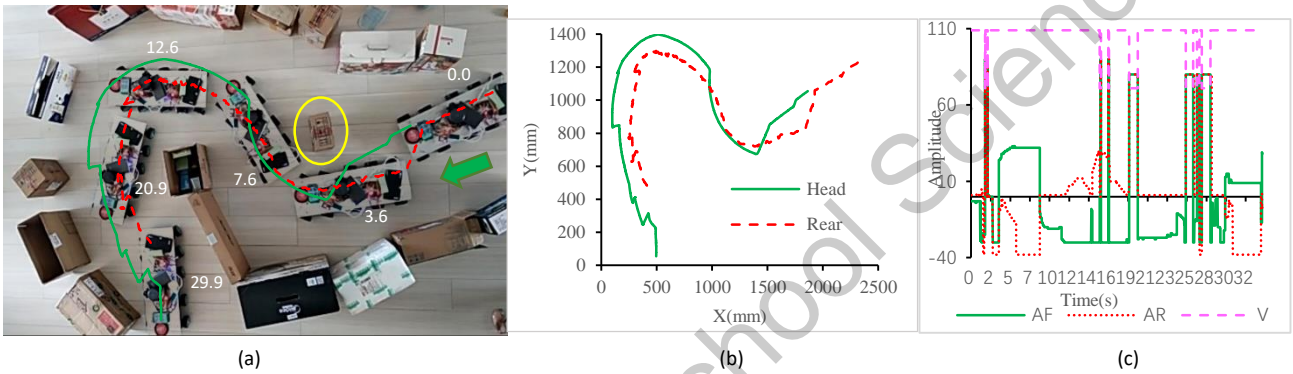


FIGURE 33: 5th Random obstacle distribution experiment. (a) Robot trajectory diagram of random obstacle avoidance. (b) Trajectory curves of head point A and rear point B of the body, and the position of A and B is shown in Figure 2. (c) Steering angles of *AF* & *AR* (The unit is degree), and speed control variable *V*.

7. Conclusion

In this article, an obstacle avoidance strategy for multi-axle long body robots is proposed, which is based on window-zone division and gap-seeking. The window-zone strategy divides the space around the robot into different areas to select lidar points, eliminate irrelevant information, and reduce the work of obstacle avoidance calculation. The specific obstacle avoidance measures are put forward when the robot is too close to the obstacle. It is based on collision level. When the distance between the robot and the obstacle is in the normal range, the gap-seeking strategy is adopted. In this strategy, the relationship between obstacles and various steering trajectory curves is calculated by double-layer iteration of front and rear steering angles to find passable channels among surrounding lidar points. Then, a five-axle all-wheel-steering wheeled robot is designed, and its obstacle avoidance control system is developed, including hardware circuit and software (control program of on-board system and upper computer). To validate the control strategy, the obstacle avoidance experiments with Z-shaped, S-shaped, U-shaped, and random distribution of obstacles were carried out. These experiments represent the typical obstacle avoidance conditions of driving in daily life. Most of the test passages are narrower than the length of the robot body. In each experiment, a special inflection point is arranged, and the robot can successfully pass it, which proves the superiority and environmental adaptability of the proposed control algorithm for multi-axle and multi-steering-mode robot to avoid obstacles in a narrow space.

References

- [1] Fatin Hassan Ajeil, Ibraheem Kasim Ibraheem, Ahmad Taher Azar, and Amjad J Humaidi, "Autonomous navigation and obstacle avoidance of an omnidirectional mobile robot using swarm optimization and sensors deployment," *International Journal of Advanced Robotic Systems*, vol. 17, pp. 1–15, 2020.
- [2] Ogren, P. , and N. E. Leonard. "Obstacle avoidance in formation." 2003 *IEEE International Conference on Robotics and Automation IEEE*, 2003.
- [3] Lee, G. , and D. Chwa., "Decentralized behavior-based formation control of multiple robots considering obstacle avoidance". *Intelligent Service Robotics*, vol. 11, pp.127-138,2018
- [4] Guo-Xing Wen and C. L. Philip Chen and Yan-Jun Liu. "Formation control with obstacle avoidance for a class of stochastic multiagent systems." *IEEE Trans. Industrial Electronics*, vol. 65, pp. 5847-5855,2018.
- [5] S. M. H. Rostami, A. K. Sangaiah, J. Wang, and H.Kim, "Real-time obstacle avoidance of mobile robots using state-dependent Riccati equation approach," *EURASIP Journal on Image and Video Processing*, vol. 2018, no.1, pp.1-13,2018.
- [6] D. Li, Z. Pan, and H. Deng, "Two-dimensional obstacle avoidance control algorithm for snake-like robot in water based on immersed boundary-lattice Boltzmann method and improved artificial potential field method," *Transactions of the Institute of Measurement and Control*, vol.42, no.10, pp.1840-1857, Jun. 2020.
- [7] D. Chen, "Fuzzy obstacle avoidance optimization of soccer robot based on an improved genetic algorithm," *Journal of Ambient Intelligence and Humanized Computing*, pp.1-12, Dec. 2019.
- [8] Rostami, S., Sangaiah, A. K., Wang, J., and Liu, X., "Obstacle avoidance of mobile robots using modified artificial potential field algorithm." *EURASIP Journal on Wireless Communications and Networking*, vol.1,2019
- [9] Y. Tao, C. Chen, T. Wang, Y. Chen, H. Xiong, F. Ren, and Y. Zou, "A re-entry path planning method for service robots based on dynamic inver-over evolutionary algorithm," *Applied Sciences*, vol.10,no.1,pp.1-15,Dec. 2019.
- [10] Ghorbani A, Shiry S, and Nodehi A, "Using Genetic Algorithm for a Mobile Robot Path Planning". *In IEEE International Conference on Future Computer and Communication*, Malaysia, pp. 164-166, 2009
- [11] Engedy I, Horvath G, "Artificial neural network based local motion planning of a wheeled mobile robot" *In IEEE International Symposium on Computational Intelligence and Informatics (CINTI).Hungary*, pp. 213-218, 2010
- [12] Garcia MP, Montiel O, Castillo O, Sepulveda R, Melin P, "Path planning for autonomous mobile robot navigation with ant colony optimization and fuzzy cost function evaluation" *Applied Soft Computing*, vol. 9,pp. 1102-1110, 2009
- [13] Montaner MB, Ramirez-Serrano A, "Fuzzy knowledge-based controller design for autonomous robot navigation" *ELSEVIER Expert Systems with Applications*, vol.14,pp.179-186, 1998.
- [14] Zhu A, and Yang SX, "Neurofuzzy-based approach to mobile robot navigation in unknown environments." *IEEE Transactions on Human-Machine Systems*,vol. 37,pp. 610-621, 2007
- [15] Miao H, and Tian YC, "Dynamic robot path planning using an enhanced simulated annealing approach." *Applied Mathematics and Computation*,vol. 222,pp. 420-437, 2013
- [16] Ahmadzadeh S, and Ghanavati M, "Navigation of mobile robot using the pso particle swarm optimization." *Journal of Academic and Applied Studies*,vol. 2,pp. 32-38, 2012
- [17] Chessa Manuela, Murgia Saverio, Nardelli Luca, Sabatini Silvio P., and Solari Fabio, "Bio-inspired active vision for obstacle avoidance," *Proceedings of the 9th International Conference on Computer Graphics Theory and Applications*, pp. 505-512, 2014.
- [18] Mon Yi-Jen, "Machine vision based sliding fuzzy-PDC control for obstacle avoidance and object recognition of service robot platform," *Intelligent and Fuzzy Systems*, vol.28,pp.1119-1126, 2015,
- [19] Bingrong Hong, Shizhao Xia, Yanqing Wang, and Ying Zhu, "Based on visual information for mobile robot dynamic obstacle avoidance," *Journal of Harbin Institute of Technology*, vol.36,pp.854-856, 2004.
- [20] Marco, D. S. , R. Zandra , and G. Domenico. "Obstacle avoidance system for unmanned ground vehicles by using ultrasonic sensors." *Machines*,vol.6,pp.18-, 2018
- [21] Fuzhong Wang, Haibo Liu, and Fashan Yu, "Strategy based on binocular stereo vision mobile robot obstacle avoidance." *Proceedings of the 27th Chinese Control Conference*, pp.457-461,2008.
- [22] Lin Chia-How, and Song Kai-Tai, "Robust ground plane region detection using multiple visual cues for obstacle avoidance of a mobile robot." *Robotica*, vol.33,pp.436-450,2015.
- [23] C. Ye and J. Borenstein, "Characterization of a 2-D laser scanner for mobile robot obstacle negotiation," *in ICRA*, pp. 2512-2518, 2002.
- [24] Peng, Y. , Qu, D. , Zhong, Y. , Xie, S. , Luo, J. , and Gu, J. , "The obstacle detection and obstacle avoidance algorithm based on 2-

D lidar." *IEEE(2015)*.

- [25] M. Takahashi, K. Kobayashi, K. Watanabe, and T. Kinoshita, "Development of prediction based emergency obstacle avoidance module by using LIDAR for mobile robot," *2014 Joint 7th International Conference on Soft Computing and Intelligent Systems (SCIS) and 15th International Symposium on Advanced Intelligent Systems (ISIS) IEEE*, pp. 561-564, 2015.
- [26] F. Fayad and V. Cherfaoui, "Tracking objects using a laser scanner in driving situation based on modeling target shape," in *Intelligent Vehicles Symposium, 2007 IEEE*, pp. 44-49, 2007.
- [27] J. Han, D. Kim, M. Lee, and M. Sunwoo, "Enhanced road boundary and obstacle detection using a downward-looking LIDAR sensor," *Vehicular Technology, IEEE Transactions on*, vol. 61, pp. 971-985, 2012.
- [28] Xing, W., He, A., Cc, A., Mz, A., Sx, A., and Yg, A., et al. "The autonomous navigation and obstacle avoidance for USVs with ANOA deep reinforcement learning method - ScienceDirect." *Knowledge-Based Systems*, 196.
- [29] Borenstein, J., and Y. Koren, "Real-time obstacle avoidance for fast mobile robots." *IEEE Transactions on Systems Man & Cybernetics* vol.19, pp. 1179-1187,2002.
- [30] T. Xu, S. Zhang, Z. Jiang, Z. Liu, and H. Cheng, "Collision avoidance of high-speed obstacles for mobile robots via maximum-speed aware velocity obstacle method," *IEEE Access*, vol.8, pp.138493-138507, 2020.
- [31] S. Zaheer, T. Gulrez, and I. A. T. Paramabath, "From sensor-space to eigenspace – a novel real-time obstacle avoidance method for mobile robots," *IETE Journal of Research*, vol.2019, pp.1-13, 2019.
- [32] C. Hu, B. Ning, M. Xu, and Q. Gu, "An experience aggregative reinforcement learning with multi-attribute decision-making for obstacle avoidance of wheeled mobile robot," *IEEE Access*, vol.8, pp.108179-108190, 2020.
- [33] K. Akka, and F. Khaber, "Optimal fuzzy tracking control with obstacles avoidance for a mobile robot based on Takagi-Sugeno fuzzy model," *Transactions of the Institute of Measurement & Control*, vol.41, pp.2772-2781, 2018.
- [34] W. Yuan, Z. Li, and C. Y. Su, "Multisensor-based navigation and control of a mobile service robot," *IEEE Transactions on Systems, Man, and Cybernetics: Systems*, vol.51, pp.2624-2634, 2019.
- [35] Yu, J., W. Hao, and W. Xin, "The research on obstacle avoidance of hospital ward inspection robots in complex environment." *2016 Chinese Control and Decision Conference (CCDC) IEEE*, 2016.
- [36] K. H. Chiang, S. H. Tseng, Y. H. Wu, G. H. Li, and L. C. Fu, "Multisensor-based outdoor tour guide robot NTU-I," in *SICE Conference IEEE*, pp. 1425-1430, Aug. 2008.
- [37] K. Zheng, F. Wu, and X. Chen, "Laser-based people detection and obstacle avoidance for a hospital transport robot," *Sensors-Basel*, vol. 21, no.3 pp.961-984, Feb. 2021
- [38] Y. Xie, X. Zhang, W. Meng, S. Zheng, and S. Wang, "Coupled fractional-order sliding mode control and obstacle avoidance of a four-wheeled steerable mobile robot," *ISA Transactions*, vol.108, pp.282–294, 2021.
- [39] Xie, H., Gao, J., Lin, Z., Zhang, C., and Luan, C., "An improved obstacle avoidance method for robot based on constraint of obstacle boundary condition" . *International Conference on Cybernetics. IEEE*.2018.
- [40] Madhavan, T. R., and M. Adharsh, "Obstacle detection and obstacle avoidance algorithm based on 2-D RPLiDAR." *2019 International Conference on Computer Communication and Informatics (ICCCI) 2019*.
- [41] W. Zheng, H. Wang, Z. Zhang, and X. Lu, "Hybrid position/virtual-force control for obstacle avoidance of wheeled robots using Elman neural network training technique," *International Journal of Advanced Robotic Systems*, vol.14, pp. 1-14, 2017.
- [42] A. A. Aldair, M. T. Rashid, and A. T. Rashid, "Navigation of mobile robot with polygon obstacles avoidance based on quadratic bezier curves," *Iranian Journal of Science and Technology, Transactions of Electrical Engineering*, vol.43, No.4, pp.757-771, Apr.2019.
- [43] P. L. Kuo, C.H. Wang, H. J. Chou, and J. S. Liu, "A real-time hydrodynamic-based obstacle avoidance system for non-holonomic mobile robots with curvature constraints," *Applied Sciences*, vol.8, pp.1-25, 2018.
- [44] R. Lin, H. Huang, and M. Li, "An automated guided logistics robot for pallet transportation," *Assembly Automation*, vol.41, pp. 45-54, 2020.
- [45] A. Prasad, B. Sharma, J. Vanualilai, and S. A. Kumar, "A geometric approach to target convergence and obstacle avoidance of a nonstandard tractor - trailer robot," *International Journal of Robust and Nonlinear Control*, vol.30, pp. 4924-4943, 2020.
- [46] P. Zhang, L. Gao, and Y. Zhu, "Study on control schemes of flexible steering system of a multi-axle all-wheel-steering robot," *Advances in Mechanical Engineering*, vol.8, pp. 1-13, 2016.

Acknowledgments

The thesis is based on daily car driving: when driving a car, the driver does not need to know in general all the distribution of obstacles around the car, but only the distribution of obstacles in the area where the car is to drive. In addition, the driver will compare the distance between the two obstacles and the width of the car to judge whether it can be passed. Therefore, I proposed an obstacle avoidance strategy based on window-zone and gap-seeking control strategy. By dividing the lidar points around the robot, the driving area is determined, and the lidar points can be screened based on this. This can greatly reduce the processing workload. Here I would like to express my heartfelt thanks to Mr. Yongqiang Zhu and Mrs. Pingxia Zhang from Qingdao University of Technology, as the instructors of this project. I am deeply impressed by their modesty, preciseness and erudition. They always take pains to solve problems when I encounter them. Mr. Zhu gave me great help and guidance from the purchase of experimental equipment at the beginning, coordination with the school on the location of experiments, determination of topics, establishment and analysis of theoretical models.

I was responsible for the manufacture, electronic control and paper writing of the obstacle avoidance control for the wheeled robot. The experimental test was completed by Mr. Zhu and me. At the same time, I also want to thank Mrs. Zhang for her guidance on experimental thinking and paper layout.

The project guidance is free of charge. Thank them very much for their hard work!

Member Introduction

Junru zhu, born in July 2004, male, student. Now I am studying at Pegasus California International School with excellent academic performance. I have a wide range of hobbies, especially small production and creations. In September 2019, an aviation club was established in our school by me, which attracted many students with the same interests to learn knowledge about aircraft and research technology of model airplanes. I also have great achievements in piano and taekwondo. I have been awarded the certificate of grade 9 by the Central Conservatory of Music and the Certificate of Black Belt (Grade 3) by the Korean Taekwondo Association. At the same time, I am full of love. In May 2020, I founded a stray animal protection organization with more than 30 members. We have held some charity activities and raised thousands of yuan for the stray dog base. The protection organization has a certain social influence, and been well received in all respects In addition, I like photography, music and have my own band.

Supervisor Introduction

Yongqiang Zhu, born in August 1975, male, associate professor, the doctor of Beijing Institute of Technology, postdoctoral of Tsinghua University and Nanyang Technological University in Singapore. In 2004, he was appointed as a lecturer and evaluated as a postgraduate tutor in 2008. In 2012, he was appointed as an associate professor. He mainly engaged in automotive dynamics, intelligent vehicle electronic control, virtual reality technology, intelligent robot design and control research and teaching. Host one item of national natural science foundation of China, participate in one item in Shandong province natural science foundation. Host and participate in over ten teaching research projects. He won two science and technology awards in Shandong Province. Be authorized 2 invention patents and 14 utility model patents. He published more than 40 papers. Participated in compiling 2 professional textbooks. He supervised 10 scientific and technological innovation projects for college students and cultivated 12 graduate students with a master's degree.

Pingxia Zhang, born in June 1973, female, assistant professor, the doctor of Beijing Institute of Technology. In 2004, she was appointed as a lecturer. She mainly engaged in automotive dynamics, intelligent vehicle electronic control, virtual reality technology, intelligent robot design and control research and teaching. Participate one item of national natural science foundation of China. Host and participate in over ten teaching research projects. Be

authorized 14 utility model patents. She published more than 40 papers. Participated in compiling 1 professional textbooks. She supervised 20 scientific and technological innovation projects for college students.

2021 S.-T. Yau High School Science Award

Paper Detection Report

文本复制检测报告单 (全文对照)

No:

检测时间: 2021-09-14 00:02:05

检测文献: Obstacle Avoidance Control

作者: 朱俊儒

检测范围: 中国学术期刊网络出版总库

中国博士学位论文全文数据库/中国优秀硕士学位论文全文数据库

中国重要会议论文全文数据库

中国重要报纸全文数据库

中国专利全文数据库

互联网资源

英文数据库(涵盖期刊、博硕、会议的英文数据以及德国Springer、英国Taylor&Francis 期刊数据库等)

港澳台学术文献库

优先出版文献库

互联网文档资源

图书资源

大成编客-原创作品库

个人比对库

时间范围: 1900-01-01至2021-09-14

检测结果

总文字复制比: 4.9%

跨语言检测结果: 0%

去除引用文献复制比: 4.9%

去除本人已发表文献复制比: 4.9%

单篇最大文字复制比: 0.7% (双车道公路长直线路段小半径曲线段限速研究)

重复字数: [2277]

总字数: [46379]

单篇最大重复字数: [305]

总段落数: [7]

前部重合字数: [339]

疑似段落最大重合字数: [581]

疑似段落数: [7]

后部重合字数: [1938]

疑似段落最小重合字数: [104]

指标: 剽窃观点 剽窃文字表述 自我剽窃

一稿多投

过度引用

整体剽窃

重复发表

表格: 0

脚注与尾注: 0

5.7% (339) Obstacle Avoidance Control_第1部分 (总5996字)

5.6% (381) Obstacle Avoidance Control_第2部分 (总6771字)

8.4% (581) Obstacle Avoidance Control_第3部分 (总6912字)

3.1% (210) Obstacle Avoidance Control_第4部分 (总6693字)

5.9% (412) Obstacle Avoidance Control_第5部分 (总6935字)

3.7% (250) Obstacle Avoidance Control_第6部分 (总6825字)

1.7% (104) Obstacle Avoidance Control_第7部分 (总6247字)

(注释: ■ 无问题部分

■ 文字复制比部分

■ 引用部分)

剽窃观点 (2)

Obstacle Avoidance Control_第2部分

1. The rest of this article is organized as follows:

Obstacle Avoidance Control_第7部分

1. to reduce the passage space here,

1. Obstacle Avoidance Control_第1部分		总字数: 5996
相似文献列表	文字复制比: 5.7%(339)	剽窃观点 (0)
1	1989IEEE - 《互联网文档资源 ()》 -	4.3% (258) 是否引证: 否
2	Int.J.Ad - 《互联网文档资源 ()》 -	1.4% (86) 是否引证: 否
3	APublica - 《互联网文档资源 ()》 -	1.4% (84) 是否引证: 否
4	Proceedi - 《互联网文档资源 ()》 -	1.4% (83) 是否引证: 否
原文内容	相似内容来源	
0	<p>此处有 144 字相似</p> <p>There are many researchers presented various algorithms, such as Genetic algorithm [10], Neural network [11], Ant colony optimization algorithm [12], Fuzzy logic [13], Neuro-fuzzy [14], Simulated annealing algorithm [15], and Particle swarm optimization algorithm [16], etc. But these studies do not consider obstacle avoidance in narrow areas.</p>	
	<p>Int.J.Ad - 《网页》 - (是否引证: 否)</p> <p>11), min-max [12], etc. The most popular of meta-heuristic algorithms are genetic algorithm [13], simulated annealing [15], ant colony optimization [14] and particle swarm optimization [16]. Braun et al.[8]</p> <p>APublica - 《网页》 - (是否引证: 否)</p> <p>2 Issue 2, February 2013, ISSN 2279-06676. CONCLUSIONS Soft computing tools are data intensive. Artificial Neural Network, Genetic Algorithm, Fuzzy Logic, Ant-colony Optimization etc. are used widely in engineering and management disciplines.</p> <p>Proceedi - 《网页》 - (是否引证: 否)</p> <p>such as Genetic Algorithms (GA), Evolutionary Programming (EP), Evolution Strategies (ES), Immune Algorithm (IA), particle swarm optimization (PSO) and Simulated Annealing (SA) [15-17]. In this paper,</p>	
1	<p>此处有 195 字相似</p> <p>Borenstein et al.[29] developed a new real-time obstacle avoidance approach for mobile robots. By permitting the detection of unknown obstacles simultaneously with the steering of the mobile robot to avoid collisions and advancing toward the target, this method can save processing time. Xu et al.[30]</p>	
	<p>1989IEEE - 《网页》 - (是否引证: 否)</p> <p>Systems, Man, and Cybernetics, Vol.19, No.5, Sept./Oct.1989, pp.1179-1187 Real-time Obstacle Avoidance for Fast Mobile Robots12 by J. Borenstein, Member, IEEE, and Y. Koren, Member, IEEE ABSTRACT A new real-time obstacle avoidance approach for mobile robots has been developed and implemented. This approach permits the detection of unknown obstacles simultaneously with the steering of the mobile robot to avoid collisions and advancing toward the target. The novelty of this approach, entitled the Virtual Force Field, lies in the integration of two known concepts: Certainty Grids for obstacle representation,</p>	
指标		
2. Obstacle Avoidance Control_第2部分		总字数: 6771
相似文献列表	5.6%(381)	

文字复制比:		剽窃观点 (0)
1	大学生论文联合库 -- 《大学生论文联合库》- 2017	1.2% (80) 是否引证: 否
2	一种中医按摩机器人控制系统的研制_自动化论文_笔耕文化传播 - 《互联网文档资源 (http://www.bigengculture.com/kejilunwen/zidonghuakongzhilunwen/1722918.html)》-	1.1% (76) 是否引证: 否
3	MEASUREM - 《互联网文档资源 ()》-	1.1% (74) 是否引证: 否
4	Internat - 《互联网文档资源 ()》-	1.1% (73) 是否引证: 否
5	Blacksil - 《互联网文档资源 ()》-	1% (68) 是否引证: 否
6	面向复杂城市环境的无人车多源信息融合导航方法研究 - 《互联网文档资源 (http://www.doc88.com/p%2D21573199902988.html)》-	0.9% (63) 是否引证: 否
7	ABSTRACT - 《互联网文档资源 ()》-	0.9% (60) 是否引证: 否

原文内容	相似内容来源
<p>0</p> <p>此处有 168 字相似</p> <p>The rest of this article is organized as follows: Firstly, the mechanical structure and hardware circuit of a lidar robot used in the obstacle avoidance experiment are analyzed in the second section. Secondly,</p>	<p>Internat - 《网页》- (是否引证: 否)</p> <p>Cube based RSA) algorithm to indicate that using hypercube to make RSA parallel is applicable. The rest of this article is organized as follows. Firstly, we describe the hypercube interconnection network in the next section. Then,</p> <p>大学生论文联合库 -- 《大学生论文联合库》-2017 (是否引证: 否)</p> <p>Obstacle avoidance technology to provide ideas. Based on the application of machine vision in intelligent obstacle avoidance robot, the mechanical structure and module circuit of the obstacle avoidance intelligent obstacle avoidance robot are designed according to the specific working requirements. The detailed design scheme of hardware circuit such as power supply module, speed detection module, motor drive module,</p>
<p>1</p> <p>此处有 213 字相似</p> <p>Fourthly, the on-board control system and the upper computer control system of the robot are introduced in the fifth section. On this basis, in order to verify the proposed methods, the experiments of obstacle avoidance with different distribution of obstacles, such as Z-shaped, S-shaped, U-shaped,</p>	<p>MEASUREM - 《网页》- (是否引证: 否)</p> <p>6) is less than the value of this function for ω_j.3. Results In order to verify the accuracy of the proposed methods simulation experiments and real images of chessboard captured by CCD camera have been used.</p> <p>ABSTRACT - 《网页》- (是否引证: 否)</p> <p>conference,8th 13th September, Penang, Malaysia grassypeptolides, hoiamides and bisebroamide. The small quantities of peptides that are produced by many marine cyanobacteria have proven to be a severe obstacle for the development of promising new leads for the development of novel drugs. In order to verify the primary structure</p>

proposed on the basis of studies of the marine peptides, and modify the structure,

一种中医按摩机器人控制系统的研制_自动化论文_笔耕文化传播 - 《网页》 - (是否引证: 否)

Finally, the design and realization of the upper computer are introduced. Finally, the system of the massage robot of traditional Chinese medicine is debugged. Taking lumbar disc herniation as an example,

面向复杂城市环境的无人车多源信息融合导航方法研究 - 《网页》 - (是否引证: 否)

Finally, the simulation and experiments are conducted to prove the proposed method. In order to verify the proposed multisensory fusion method, on the basis of the above schemes and algorithms, the car-mounted testbed is built and field tests are carried out.

指标

3. Obstacle Avoidance Control_第3部分

总字数: 6912

相似文献列表	文字复制比: 8.4%(581)	剽窃观点 (0)
1	AthensJo - 《互联网文档资源 ()》 -	1.5% (104) 是否引证: 否
2	ISSN:227 - 《互联网文档资源 ()》 -	1.4% (97) 是否引证: 否
3	CT6DRIV - 《互联网文档资源 ()》 -	1% (68) 是否引证: 否
4	10thESAW - 《互联网文档资源 ()》 -	1% (67) 是否引证: 否
5	AllThese - 《互联网文档资源 ()》 -	1% (67) 是否引证: 否
6	ONeill, - 《互联网文档资源 ()》 -	1% (66) 是否引证: 否
7	Foryours - 《互联网文档资源 ()》 -	0.9% (65) 是否引证: 否
8	基于后轮主动转向系统高速汽车侧风稳定性研究 - 道客... - 《互联网文档资源 (https://www.doc88.com/p%2D8476427449130.html)》 -	0.9% (61) 是否引证: 否
9	ESP 汽车英语 中英对照 Unit5 passageB 高等教育出版社 - 《互联网文档资源 ()》 -	0.9% (59) 是否引证: 否

原文内容	相似内容来源
<p>0 此处有 209 字相似</p> <p>Where is the distance between the turning center point O and the first axle of the robot projected on the longitudinal center line of the robot. and are the steering angles of the front and rear virtual wheels on the center of the first axle and last axle, respectively. The unit is degree. When the wheels are steering clockwise,</p>	<p>Foryours - 《网页》 - (是否引证: 否)</p> <p>4WAS) system is an electronically controlled four-wheel steering system. Depending on the vehicle speed and steering angle, the angles of the front and rear wheels are adjusted by the 4WAS system to help improve driving performance. If a malfunction occurs in the system,</p> <p>AthensJo - 《网页》 - (是否引证: 否)</p>

		<p>As Fig.6 demonstrates, the geometric relationship of the distance between the global center point of the robot and the axle of the rotating contact wheel is given by:(12)</p> <p>AllThese - 《网页》 - (是否引证: 否)</p> <p>4 Figure 4. Focal length (f) is the distance between ions turning point and the center of the EIBT. Focal length (f) is the distance between ions turning point and the center of the EIBT. Vs represents the highest voltages in the electrostatic mirror.</p>
1	<p>此处有 98 字相似</p> <p>Since the radius of the track circle of each wheel is different when turning, the speed of the wheel is also different, and is proportional to the radius of the track circle. According to the size of the moving radius,</p>	<p>ESP 汽车英语 中英对照 Unit5 passageB 高等教育出版社 - 《网页》 - (是否引证: 否)</p> <p>束的调整由调整转向杆系来实现,前束非常重要是因为不合适的前束可以引起轮胎的非正常磨损和轮胎的使用时间短缩。 Toe-out. When an automobile turns a corner, the radius of the turning circle of the inner wheel is smaller than that of the outer wheel. The wheels must, therefore,</p>
2	<p>此处有 124 字相似</p> <p>In this way, according to Ackerman's theorem, we can calculate the steering angles and speed of the robot's all actual wheels according to the steering angles of the two virtual wheels: AF and AR.</p> <p>According to the need of obstacle-avoiding steering of the robot, the following steering modes are proposed based on the front and rear virtual wheels steering angles AF and AR and moving speed V:</p>	<p>10thESAW - 《网页》 - (是否引证: 否)</p> <p>IRC) is located at the middle wheel axle of the rover, the IRC is dened by the steering angle α of the virtual wheel and the rover dimensions. The angles of the steering wheels and the rotational speeds of the driving wheels depend on the rotational speed v and the steering angle α of the virtual wheel:$\beta_i = f(\alpha)$, $v_i = f(v, \alpha)$. Figure 9: Table showing the input parameters for the MMI GUI Ackermann Mode Turn on Spot Mode Lateral</p>
3	<p>此处有 150 字相似</p> <p>This is the adverse-phase steering mode, as shown in Figure 5. At this point, the steering direction of the front and rear virtual wheels is opposite, and the actual steering direction of the front and rear wheels of the robot is also opposite. The robot can have a relatively small turning radius. Space used for steering is also small. Therefore,</p>	<p>ISSN:227 - 《网页》 - (是否引证: 否)</p> <p>when added to this system, it will further improve maneuverability and drivers ease of access. By steering the rear wheels in the direction opposite the front wheels at low speeds, the vehicles turning circle radius is greatly reduced. Therefore,</p> <p>基于后轮主动转向系统高速汽车侧风稳定性研究 - 道客... - 《网页》 - (是否引证: 否)</p> <p>butalso the rear wheel can participate in steering.When the speed is low, the turning radius ofthe front and rear wheels of the vehicle is opposite and the turning radius is reduced, andthe maneuverability of the vehicle is improved,</p> <p>ONeill, - 《网页》 - (是否引证: 否)</p> <p>Swing-out is more evident in low speed manoeuvring, where 2http www.bmw.com 3Negative phase is steering the rear wheels in the opposite direction to the front wheels CHAPTER 1.</p> <p>CT6DRIVI - 《网页》 - (是否引证: 否)</p> <p>The result is a smooth, responsive drive. A MORE</p>

SUPPLE TURN For more agility at low speeds, **Active Rear Steering turns the rear wheels in the opposite direction to the front wheels.** This shortens the turning circle and makes parking and slow-speed maneuvering much easier.

指标	
4. Obstacle Avoidance Control_第4部分	
总字数: 6693	
相似文献列表	文字复制比: 3.1%(210) 剽窃观点 (0)
1 <u>Caterpil</u> - 《互联网文档资源 ()》 -	1.3% (90) 是否引证: 否
2 <u>双开口Helmholtz局域共振周期结构低频带隙特性研究_化学论文_笔耕文化传播</u> - 《互联网文档资源 (http://www.bigengculture.com/kejilunwen/huaxue/1612496.html)》 -	1% (66) 是否引证: 否
3 <u>AMATHEMA</u> - 《互联网文档资源 ()》 -	0.8% (56) 是否引证: 否

原文内容	相似内容来源
<p>此处有 210 字相似</p> <p>For the lidar points at both sides of the gap, as shown in Figure16(a), the one close to the longitudinal center line of the robot body is the inside point, and the one is far away from the longitudinal center line of the robot body is the outside point. Then, the distance between the inside point of the gap and the turning center O is (in mm):</p>	<p>Caterpil - 《网页》 - (是否引证: 否)</p> <p>and the load is applied at a point on the longitudinal center line of the machine at half the distance from the most rearward point of the load opening to the tip of the fork,</p> <p>AMATHEMA - 《网页》 - (是否引证: 否)</p> <p>PX 'Y' is the coordinate system fixed to the mobile robot; P is the middle of the rear axis; Pc is the center of mass of the robot body; d is the distance between P and Pc;2b is the distance between the two driving wheels, e.g., length of the rear axis;</p> <p>双开口Helmholtz局域共振周期结构低频带隙特性研究_化学论文_笔耕文化传播 - 《网页》 - (是否引证: 否)</p> <p>inner arc length is longer, the low frequency band gap is low; the greater the distance between the inside and outside the cavity, thereby The cavity volume becomes smaller, the band gap moves to high frequency,</p>

指标	
5. Obstacle Avoidance Control_第5部分	
总字数: 6935	
相似文献列表	文字复制比: 5.9%(412) 剽窃观点 (0)
1 <u>基于ARM与FPGA的并条机自调匀整控制系统研究与实现_知识产权法论文_笔耕文化传播</u> - 《互联网文档资源 (http://www.bigengculture.com/falvlunwen/zhishichanquanfa/2340073.html)》 -	1.6% (111) 是否引证: 否
2 <u>基于MCP2515的CAN总线通信单元设计</u> - 《互联网文档资源 ()》 -	1.1% (75) 是否引证: 否
3 <u>大学生论文联合库</u> -- 《大学生论文联合库》 - 2017	1% (71) 是否引证: 否
4 <u>Journalo</u> - 《互联网文档资源 ()》 -	1% (70) 是否引证: 否

5	大学生论文联合库 裴雄 - 《大学生论文联合库》 - 2017	1% (69) 是否引证: 否
6	双车道公路长直线接小半径曲线路段限速研究 方超;袁方;宗卫锋;郭内强;郭忠印;李志勇 - 《公路工程》 - 2018	0.9% (62) 是否引证: 否

	原文内容	相似内容来源
0	<p>此处有 107 字相似</p> <p>The whole control system of the obstacle avoidance robot is mainly composed of software control program and hardware circuit. The software control program is divided into an on-board control system program and upper computer program.</p>	<p>基于ARM与FPGA的并条机自调匀整控制系统研究与实现_知识产权去论文_笔耕文化传播 - 《网页》 - (是否引证: 否)</p> <p>and expounds the overall structure of the control system in detail. The control system is mainly composed of hardware circuit and software program. After the system structure is clear,</p> <p>大学生论文联合库 裴雄-《大学生论文联合库》-2017 (是否引证: 否)</p> <p>.The main idea of my design is the ultrasonic level detector based on MCU. It is composed of hardware circuit and software program. The hardware mainly uses AT89C51 chip as the core to complete the ultrasonic liquid level measurement and data processing.</p>
1	<p>此处有 305 字相似</p> <p>calculate the information of obstacles, and display the relevant information through the touch screen. At the same time, the lidar information is sent to the upper computer through WIFI, and the robot obstacle avoidance steering and speed control instructions sent by the upper computer are received through WIFI. These instructions are decomposed into the steering angle and wheel speed of 10 wheels. Robot on-board control system procedures include:</p>	<p>Journalo - 《网页》 - (是否引证: 否)</p> <p>and compared with the default values then decided to do the corresponding action or not. At the same time, the system display relevant content according to the touch screen operation and monitor network.</p> <p>大学生论文联合库 -- 《大学生论文联合库》-2017 (是否引证: 否)</p> <p>The controller is the device that receives the information sent by the upper computer to the wheeled robot. Then the information is converted to make wheeled robots action..</p> <p>基于MCP2515的CAN总线通信单元设计 - 《网页》 - (是否引证: 否)</p> <p>convenient use. To realize the design of CAN bus communication unit based on this interface chip, the DSP + FPGA framework is adopted in this design. The SPI interface logic and MCP2515 instruction transformation logic are achieved in FPGA to accomplish the different SPI commands. The upper computer instructions are received and the control to MCP2515 is finished in DSP.</p> <p>双车道公路长直线接小半径曲线路段限速研究 方超;袁方;宗卫锋;郭内强;郭忠印;李志勇-《公路工程》-2018 (是否引证: 否)</p> <p>The dynamic response.data of vehicle speed and steering wheel angle of 10 drivers driving in 5 kinds of small radius curve.scenes on the driving simulation platform were collected.The variation</p>

of speed and steering wheel angle.in curve were analyzed.Then the minimum speed logarithm regression model was established.

指标	
6. Obstacle Avoidance Control_第6部分	
总字数: 6825	
相似文献列表	文字复制比: 3.7%(250) 剽窃观点 (0)
1	智能小车单目视觉障碍检测及避障系统设计 闵小;李迎;李蒙;陈刚 - 《电子技术(上海)》- 2018 1.1% (75) 是否引证: 否
2	基于物联网的智能花卉培育系统 - 道客巴巴 - 《互联网文档资源 (http://www.doc88.com/p%2D4127802948976.html) 》 - 1.1% (73) 是否引证: 否
3	JanRompo - 《互联网文档资源 () 》 - 1% (65) 是否引证: 否
4	STATEOFC - 《互联网文档资源 () 》 - 0.9% (64) 是否引证: 否
5	Asof2018 - 《互联网文档资源 () 》 - 0.9% (62) 是否引证: 否
原文内容	相似内容来源
<p>此处有 148 字相似</p> <p>is the percentage of the number of obstacle avoidance computations in the corresponding ith period of time to the total number of obstacle avoidance computations in the entire obstacle avoidance process. is the number of times in the period of the obstacle avoidance calculation cost. The time periods are</p>	<p>JanRompo - 《网页》 - (是否引证: 否)</p> <p>in order to get an approximate speedup. In the specic case of the obstacle avoidance model, the total number of programs is 41[19]. Hence,</p> <p>Asof2018 - 《网页》 - (是否引证: 否)</p> <p>is, for the entire period,\$100 times the number of acres of that type of land. Basic tax reduction: eligible former grazing area 5(2) Subject to subsection (4), the basic tax reduction for riparian land that is an eligible former grazing area throughout the benefit period is, for the entire period, the following amount times the number of acres of that type of land:(a)\$140,</p> <p>STATEOFC - 《网页》 - (是否引证: 否)</p> <p>times (b) Federal Funds Effective Rate or Interest Rate, as applicable; times (c) The result of dividing the number of days in the calculation period by 360.242."Site" means the real property on which the Generating Facility is, or will be located,</p>
<p>此处有 102 字相似</p> <p>These cases are up to 96% in the total number of obstacle avoidance counts. It shows that the time response of this algorithm is very fast and meets the requirement of real-time obstacle avoidance. In addition, as the width of the passage narrows, the percentage of each obstacle avoidance calculation time less than 10ms becomes smaller during the entire obstacle avoidance process. This indicates that the narrower the passage, the larger the steering angle, and the more iterations. As a result, for each obstacle distribution information collected</p>	<p>基于物联网的智能花卉培育系统 - 道客巴巴 - 《网页》 - (是否引证: 否)</p> <p>548ms to process a medi—um size image averagely.Its accuracy is larger than 95%.The algorithm is fast and robust.It meets the real time requirement of pick—ing robot.Keywords:machine vision;color segment;edge tracking;circle detection(上接第82页)</p> <p>智能小车单目视觉障碍检测及避障系统设计 闵小; 李迎; 李蒙; 陈刚-《电子技术(上海)》-2018 (是否引证: 否)</p>

by lidar, the corresponding obstacle avoidance calculation time is more.	can realize .detection and obstacle avoidance based on monocular vision, and meets the requirement of real-time obstacle .avoidance. Real-time obstacle avoidance requirements..Key words:
--	---

指标	
7. Obstacle Avoidance Control_第7部分	
总字数: 6247	
相似文献列表	文字复制比: 1.7%(104) 剽窃观点 (0)
1 Effectof - 《互联网文档资源 ()》-	1.1% (67) 是否引证: 否
2 Genetics - 《互联网文档资源 ()》-	1% (62) 是否引证: 否
原文内容	相似内容来源
<p>此处有 104 字相似</p> <p>a) to reduce the passage space here, change the curve shape of the passage, and increase the difficulty of obstacle avoidance. The robot enters from the right side of the figure. It can be seen from Figure 33(b), the trajectory curves change sharply, indicating that the robot can adapt to sharp channel changes and realize sharp turn to avoid obstacles. It can be seen from Figure 33(c), the robot repeatedly moved to the left and back with the wheel control variables AF and AR of 80° and the speed V of 71. In this way, it can avoid obstacles on the right side and adjust the body posture to pass through the channel with drastic change.</p>	<p>Genetics - 《网页》- (是否引证: 否)</p> <p>the rate of lesion size increase, and the shape of the lesion size increase curve would change. The fact that lesion growth rates differ and the increase is not always linear implies that multiple measurements are needed for accurate assessment of reaction to E. turcicum. A genetic interaction with time exists, because response curves differ with genotype.</p> <p>Effectof - 《网页》- (是否引证: 否)</p> <p>the presence of a double peak and the increase of the transition temperature. The change of the curve shape after Tc for the WBIT-2Zn_RS sample becomes a clear shoulder for the sample WBIT-5Zn_C.</p>

指标

- 说明:
- 1.指标是由系统根据《学术论文不端行为的界定标准》自动生成的
 - 2.红色文字表示文字复制部分,绿色文字表示引用部分
 - 3.本报告单仅对您所选择对比资源范围内检测结果负责